

REVIEW ARTICLE

Open Access

Recent progress in the development of high-efficiency inverted perovskite solar cells

Sanwan Liu¹, Vasudevan P. Biju^{2,3}, Yabing Qi⁴, Wei Chen^{1,5} and Zonghao Liu^{1,5}

Abstract

Perovskite solar cells (PSCs) have attracted much attention due to their low-cost fabrication and high power conversion efficiency (PCE). However, the long-term stability issues of PSCs remain a significant bottleneck impeding their commercialization. Inverted PSCs with a p-i-n architecture are being actively researched due to their concurrent good stability and decent efficiency. In particular, the PCE of inverted PSCs has improved significantly in recent years and is now almost approaching that of n-i-p PSCs. This review summarizes recent progress in the development of high-efficiency inverted PSCs, including the development of perovskite compositions, fabrication methods, and counter electrode materials (CEMs). Notably, we highlight the development of charge transport materials (CTMs) and the effects of defect passivation strategies on the performance of inverted PSCs. Finally, we discuss the remaining issues and perspectives of high-efficiency inverted PSCs.

Introduction

Perovskite solar cells (PSCs) have attracted extensive research attention due to their excellent photoelectric properties and low-cost fabrication. The power conversion efficiency (PCE) of PSCs has increased to an impressive value of 25.7% after more than ten years of development¹. PSCs are a new-generation photovoltaic technology whose efficiency is quickly increasing, indicating their potential for subverting the photovoltaic market. PSCs with a certified efficiency exceeding 25% have n-i-p structures^{2–4}, which are categorized into mesoporous and regular structures (Fig. 1). The difference between the two structures is that the former collects the carriers generated in a perovskite layer. In the early stage of PSC development, most PSCs were designed with a dense TiO₂ layer with an additional mesoporous TiO₂ layer as an electron transport material (ETM)^{5,6}, requiring high-temperature processing, and the corresponding

devices showed high hysteresis. These drawbacks increased the fabrication cost of mesoporous PSCs and hindered their further development. Then in the later stage of PSC development, SnO₂ with excellent photoelectric properties prepared by a low-temperature process was used as an ETM to produce PSCs with better performance^{7–10}. The world record for PSC efficiency was achieved with a PSC based on a SnO₂-based regular structure^{2–4,9}. However, regular PSCs still face the problems of high hysteresis and insufficient stability^{11,12}. In particular, hygroscopic lithium salt-doped 2,2',7,7'-tetrakis[N,N-bis(p-methoxyphenyl)amino]-9,9'-spirobifluorene (spiro-OMeTAD) as the hole-transport layer in PSCs with record efficiencies is not sufficiently stable, which essentially limits the long-term stability of the corresponding devices^{13,14}.

In contrast, PSCs based on inverted (p-i-n) planar structures (Fig. 1c) using intrinsically stable electron charge transport layers, such as [6,6]-phenyl-C61-butyric acid methyl ester (PCBM) or C₆₀, and stable metal electrodes have demonstrated good stability, low hysteresis, and competitive efficiency, making p-i-n PSCs a promising architecture for future practical applications^{15–20}. Moreover, p-i-n PSCs are also promising for use in

Correspondence: Vasudevan P. Biju (biju@es.hokudai.ac.jp) or Yabing Qi (Yabing.Qi@OIST.jp) or Zonghao Liu (liuzonghao@hust.edu.cn)
¹Wuhan National Laboratory for Optoelectronics (WNLO), Huazhong University of Science and Technology (HUST), Wuhan, China
²Research Institute for Electronic Science, Hokkaido University, Sapporo, Hokkaido, Japan
Full list of author information is available at the end of the article

© The Author(s) 2023

 **Open Access** This article is licensed under a Creative Commons Attribution 4.0 International License, which permits use, sharing, adaptation, distribution and reproduction in any medium or format, as long as you give appropriate credit to the original author(s) and the source, provide a link to the Creative Commons license, and indicate if changes were made. The images or other third party material in this article are included in the article's Creative Commons license, unless indicated otherwise in a credit line to the material. If material is not included in the article's Creative Commons license and your intended use is not permitted by statutory regulation or exceeds the permitted use, you will need to obtain permission directly from the copyright holder. To view a copy of this license, visit <http://creativecommons.org/licenses/by/4.0/>.

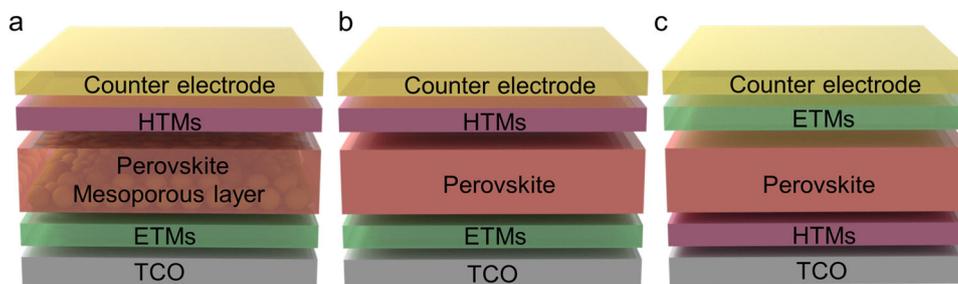


Fig. 1 Device structures of PSCs. **a** Mesoporous structure. **b** Regular n-i-p structure. **c** Planar p-i-n (inverted) structure.

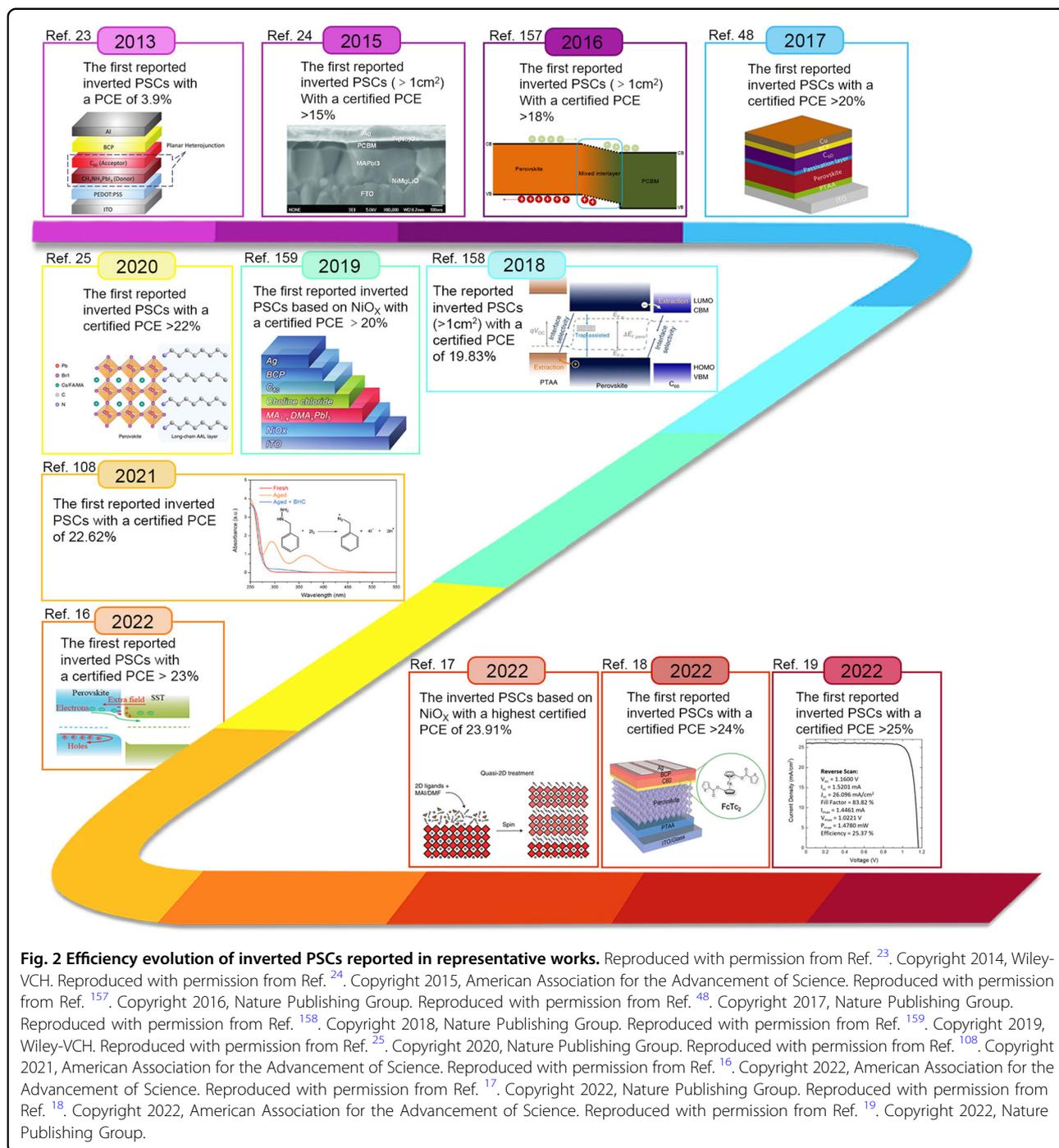
tandem solar cells^{21,22}. However, there is still a gap between inverted PSCs and regular PSCs in terms of efficiency. Therefore, most studies on inverted PSCs in the past decade have focused on improving their PCE.

Figure 2 shows the key progress in research on the efficiency of inverted PSCs. The first inverted PSC was reported in 2013 with an efficiency of 3.9%²³. Two years later, the first 1 cm² inverted PSC with a record PCE of 15% was reported and showed excellent light stability for over 1000 h²⁴, which triggered an upsurge in research on improving the efficiency of inverted PSCs. After several years of development, the certified PCE of inverted PSCs exceeded 22% in 2020 for the first time²⁵. Subsequently, the certified PCE of inverted PSCs surpassed 23%, 24%, and 25% in 2022^{16–19}. Moreover, inverted perovskite mini-modules achieved certified PCEs of 19.2% with an aperture area of 50 cm² in 2021 and 21.07% with an aperture area of 12.84 cm² in 2022^{26,27}, which are approaching the record efficiency of regular mini-modules²⁸. Note that inverted PSCs could maintain 95% of their initial efficiency after over 1000 h under damp-heat test conditions recently stipulated by the standards of IEC 61215:2016^{18,20}. The above progress fully illustrates that inverted PSCs have more advantages in fabricating efficient and stable small-area PSCs and large-area modules, which means that inverted PSCs have more potential for industrialization. Detailed performance parameters of representative inverted PSCs are summarized in Table 1.

We focus on the recent progress in high-efficiency inverted PSC research. The rapid increases in the efficiency and stability of inverted PSCs prompted us to summarize their current progress, including the development of perovskite compositions, fabrication methods, and counter electrode materials (CEMs). In particular, we highlight the development of charge transport materials and the effects of defect passivation strategies on the performance of inverted PSCs. Finally, we provide conclusions and insights regarding stability and efficiency in terms of reducing the cost of materials and realizing the commercialization of inverted PSCs.

Perovskite compositions and fabrication methods

As the light-absorbing layer, a perovskite film has an important impact on the performance of inverted PSCs. A compact and uniform perovskite film is the key requirement for preventing undesirable contact between the upper and lower charge transport layers (CTLs). Additionally, high-quality films are essential for reducing interfacial nonradiative recombination due to defects and interface mismatch energy levels, which severely limit the open circuit voltage (V_{OC}) and fill factor (FF) values of PSCs^{29,30}. Considerable efforts have been made to improve perovskite films quality, including fabrication method optimization, band gap tuning, and defect passivation. The PCE of PSCs containing an appropriate-band-gap perovskite is expected to exceed 30% based on the Schottky-Queisser (S-Q) limit³¹, which can be achieved by adjusting the perovskite composition. The perovskites of high-efficiency inverted PSCs have changed from the initial methylammonium lead iodide (CH₃NH₃PbI₃, MAPbI₃) to formamidinium (FA)-based perovskites, including double-cation (FAMA) perovskite, triple-cation (cesium (Cs)FAMA) mixed-halide perovskite, and FA-Cs mixed-cation perovskites^{32–35}. The fabrication methods of perovskite films have also changed to accommodate these different perovskite compositions. Currently, the mainstream method for fabricating inverted PSCs is a one-step method that readily provides dense and uniform high-quality perovskite films^{36–38}. The two-step solution method commonly used for regular PSCs is not suitable for inverted perovskite films because the complete conversion of PbI₂ into perovskite is strongly dependent on the fabrication conditions. The resulting perovskite films are usually very rough, making it difficult for a thin PCBM or C₆₀ layer to fully cover the bottom perovskite layer and thus leading to serious charge carrier loss³⁹. Different from those used to fabricate lab-scale small-area cells, scalable fabrication methods, such as vacuum deposition, blade coating, and slot-die coating, are usually used to fabricate large-area perovskite solar modules^{40–42}. This section summarizes the perovskite compositions and fabrication methods of high-efficiency inverted PSCs.



Unless otherwise stated, the perovskite compositions discussed in this review are all lead-based perovskite compositions.

Development of perovskite compositions

The most popular perovskite composition in early inverted PSCs was MAPbI₃. However, MAPbI₃ is not suitable for practical application due to its thermal

instability⁴³, including its volatility and intrinsic instability caused by reversible/irreversible decomposition reactions even at low temperatures³³. The FA cation exhibits better thermal stability because of its stronger hydrogen bonding with PbX₆ octahedra than the MA cation. It initiates a reversible decomposition reaction below 85 °C^{44,45} and has gradually become the main cation in almost all high-performance inverted PSCs. Researchers found that the

Table 1 Summary of the solar cell performance parameters reported in representative studies on inverted PSCs (note that perovskite is abbreviated as PVK).

Perovskite	Device structure	Active area (cm ²)	V _{oc} (V)	J _{sc} (mA cm ⁻²)	FF (%)	PCE (%)	References
MAPbI ₃	ITO/PEDOT:PSS/PVK/C ₆₀ /BCP/Al	0.06	0.60	10.32	58	3.9	23
MAPbI ₃	FTO/NiMgLiO/PVK/PCBM/PTI(Nb)/O _x /Ag	1.017	1.072	20.62	74.8	16.2	24
MAPbI ₃	FTO/NiMgLiO/PVK/PCBM/PCBM/TTI(Nb)/O _x /Ag	1.022	1.08	21.98	79	18.75	157
FA _{0.85} MA _{0.15} PbI ₃	ITO/PTAA/PVK/Choline chloride/C ₆₀ /BCP/Cu	0.0716	1.14	23.7	78	21.0	48
(CsPbI ₃) _{0.05} [(FAPbI ₃) _{0.85} (MAPbBr ₃) _{0.1}] _{0.95}	ITO/PTAA/PEN-P2/PVK/LiF/C ₆₀ /BCP/Cu	1.018	1.132	22.24	80.5	20.3	158
MA _{0.89} DMA _{0.11} PbI ₃	ITO/NiO _x /PVK/Choline chloride/C ₆₀ /BCP/Ag	0.04	1.116	23.5	82	21.6	159
C ₅₀ 05(F _{A0.92} M _{A0.08}) _{0.95} PbI ₃	ITO/PTAA/PVK/C ₆₀ /BCP/Cu	0.1	1.17	24.1	81.6	23.0	25
C ₅₀ 05(F _{A0.95} M _{A0.05}) _{0.95} PbI ₃	ITO/PTAA/PVK/C ₆₀ /BCP/Ag	0.073	1.17	23.9	83.6	23.4	108
(FAPbI ₃) _{0.95} (MAPbBr ₃) _{0.05}	ITO/P3CT-N/PVK/PCBM/C ₆₀ /TPBi/Cu	0.09	1.19	24.8	82.9	24.3	16
C ₅₀ 05F _{A0.85} M _{A0.15} PbI ₃	ITO/NiO _x /PVK/3F-PEAI/PCBM/BCP/Ag	0.053	1.15	24.90	83.46	23.91	17
C ₅₀ 05(F _{A0.98} M _{A0.02}) _{0.95} PbI ₃	ITO/PTAA/PVK/FcTc ₂ /C ₆₀ /BCP/Ag	0.08	1.184	25.68	82.32	25.0	18
Rb _{0.05} Cs _{0.05} MA _{0.05} FA _{0.85} PbI ₃	ITO/MeO-2PACZ/PVK/3-APy/LiF/C ₆₀ /BCP/Ag	0.112	1.16	26.10	83.82	25.37	19

PFM-P2 poly[(9,9-bis(30-(N,N-dimethyl)-N-ethylammonium)-propyl)-2,7-fluorene]-alt-2,7-(9,9-dioctylfluorene)] dibromide, 3F-PEAI 3-fluoro-phenethylammonium, P3CT-N Poly[3-(4-carboxylatebutyl)thiophene]-CH₃NH₂.

short circuit current (J_{SC}) could be increased by replacing MA⁺ with FA⁺ in perovskites for inverted PSCs because FA⁺ could narrow the band gap and expand the absorption range of perovskite films^{46,47}. Huang et al. partially replaced MA with FA to obtain FA_{0.85}MA_{0.15}PbI₃ as the light-absorbing layer, and the J_{SC} of the corresponding PSC was approximately 1 mA cm⁻² higher than that of the MAPbI₃-based PSC⁴⁸, thereby improving the device performance. In addition, Zhu et al. systematically compared the effects of different perovskite compositions on device performance. They found that the J_{SC} of FA-based PSCs was significantly higher than that of MA-based PSCs (25.38 versus 23.26 mA cm⁻²)¹⁸. Furthermore, when MA⁺ was partly replaced with Cs⁺, Cs⁺ effectively controlled the crystallization rate by increasing the entropy of crystallization, thereby improving the perovskite film quality⁴⁹. In addition, researchers proved that the size mismatch between Cs⁺ and FA⁺ induced chemical pressure and lattice strain, resulting in octahedral tilting and stronger N–H...I hydrogen bonding between FA⁺ and I⁻, which reduced the vibrational intensity and improved the thermal stability of the perovskite structure^{50,51}.

Moreover, to approach the ideal band gap of 1.34 eV according to the S-Q limit, commonly used perovskite compositions have evolved from the initial MAPbI₃ to double-cation FAMA or FACs, triple-cation CsMAFA, and quadruple-cation (rubidium-(Rb)-CsMAFA, CsFAMA-guanidinium (GUA)^{19,52}-based perovskites. Pure FAPbI₃ has an ideal narrow band gap. FA, which has been successfully applied in regular PSCs, is the largest organic cation suitable for the three-dimensional (3D) perovskite crystal structures that are widely used as light-absorbing layers in high-efficiency regular PSCs^{3,4}. However, pure FAPbI₃ is rarely used as a photoactive layer in inverted PSCs due to its intrinsic poor phase stability and the difficulty of crystallizing α -FAPbI₃. Therefore, various effective strategies have been reported for stabilizing the black phase of FAPbI₃ and improving the crystallinity and morphology of perovskite films^{53,54}. In these strategies, methylammonium chloride (MAcI) is the most commonly used additive for achieving high-quality black-phase FAPbI₃ crystallization via the formation of an intermediate phase and has been successfully applied to improve the efficiency of regular-structure devices^{55–57}. However, it was reported that the optimal annealing temperature of FAPbI₃ is lower than that of regular-structured PSCs (150 °C), which is not the ideal annealing temperature of FAPbI₃⁵⁸. In addition, residual additive destabilizes the film and can form a nonradiative recombination center in the final FAPbI₃ film^{58,59}. Although the efficiency of inverted PSCs with FAPbI₃ based on self-assembled monolayers (SAMs) slightly exceeded 22%⁵⁸, it

still lags behind inverted PSCs with quadruple cations or triple cations as the perovskite active layer (PCE > 25%)^{18,19}. Therefore, compared with double cations or triple cations, FAPbI₃ is not competitive as the photoactive layer in terms of the difficulty of fabricating perovskite films and the lower efficiency and stability of the final device.

Development of perovskite fabrication methods

A compact, uniform, and high-quality perovskite film is the key requirement for preventing current leakage generated by undesirable contact between the ETMs and the hole transport materials (HTMs) and facilitating efficient charge generation and collection. Fabrication methods can affect the film quality and device performance. It is crucial to select suitable film fabrication methods for obtaining high-efficiency PSCs. A myriad of film fabrication methods have been used for inverted PSCs. The following section elucidates four commonly used fabrication methods for high-efficiency inverted PSCs.

Vacuum deposition

During vacuum deposition, the precursor materials are thermally evaporated and then reacted to form perovskite films on a substrate. Regardless of the wettability of the substrate surface, the vacuum deposition method ensures the fabrication of conformal, dense, and uniform perovskite films⁶⁰. Compared with the advantages of the solution method, another key advantage of vacuum deposition is the accurate control over the film thickness and morphology required to provide sufficient spatial performance uniformity even for large-scale PSC modules. For example, Bolink et al. systematically studied the effect of perovskite film thickness on the performance of inverted PSCs and achieved an efficiency of 16.5% without hysteresis with a 500 nm-thick MAPbI₃ layer⁶¹. In addition, Stranks et al. reported a multisource vacuum deposition method for obtaining high-quality FA_{0.7}Cs_{0.3}Pb(I_{0.9}Br_{0.1})₃ perovskite films with good film morphology and photoelectric properties, which enabled them to control the addition of excessive PbI₂ during vacuum deposition and achieve a stable power output efficiency of 18.2% for their inverted PSCs⁶². In addition to obtaining perovskite films by vacuum deposition, Park et al. deposited an n-butylammonium bromide (BABr)-based passivation layer at the perovskite/PCBM interface by vacuum deposition. They achieved an impressive efficiency of 21.4% for their inverted PSCs⁶³.

Although vacuum deposition has been successfully applied, high energy consumption, high cost, complexity, and low raw material utilization are a few factors limiting its wide use in practical manufacturing processes. Moreover, the crystalline quality of perovskite films fabricated by vacuum deposition is still insufficient. Compared to

vacuum deposition, the two-step, and one-step solution methods exhibit advantages such as simple and low-cost fabrication. These methods are discussed in the following section.

Two-step solution method

The two-step solution method, which allows more flexible modulation of perovskite crystallization than the one-step method, has been intensively studied for regular PSCs. It is easier to control the growth of a single component in the perovskite precursor than it is to control that of multiple components⁶⁴. When the two-step solution method is used to fabricate a planar structure, PbI₂ tends to form a dense film. The subsequent organic cation solution has difficulty penetrating the PbI₂ film and usually only reacts with the surface of the PbI₂ film, resulting in residual PbI₂ in the final perovskite film. Excess PbI₂ positively reduces interfacial charge recombination in regular PSCs, and recent studies have also revealed that excess PbI₂ is detrimental to the long-term stability of PSCs. In addition, the photolysis of excess PbI₂ into metallic Pb and I₂ under light illumination increases the charge transfer resistance of inverted PSCs. Therefore, achieving the full conversion of PbI₂ to perovskite is the main challenge of the “two-step” method for inverted PSCs. To solve this problem, Huang et al. improved the traditional two-step method for inverted PSCs (Fig. 3a)⁶⁵. In brief, an MAI solution was spin-coated on top of the PbI₂ layer to form stacked films. MAI diffused into and reacted with PbI₂ to form MAPbI₃ during the thermal annealing process. The full conversion of PbI₂ to perovskite was achieved by precisely controlling the thickness of the films. With the help of solvent annealing, this method produced high-quality perovskite films with larger grain sizes. The resulting PSCs achieved a high efficiency of 15.6% with a high FF of 77.5%. Around the same time, Wu et al. reported that the addition of a small amount of H₂O into PbI₂/dimethylformamide (DMF) solution produced high-quality PbI₂ films (Fig. 3b). The PbI₂ film prepared from PbI₂/DMF containing 2 wt% water (denoted as PbI₂-2) was a smooth and continuous film with full coverage⁶⁶. The PbI₂-2-based perovskite films fabricated by the two-step method were compact and smooth without pinholes. Consequently, the corresponding champion cell achieved an impressive PCE of 18% with a remarkable FF of 0.85. They also used DMF vapor post-treatment in the perovskite annealing process and obtained high-quality perovskite films with large grain sizes, which enlarged the shunt resistance and suppressed carrier recombination at the interfaces, resulting in high J_{SC} and V_{OC} values. Consequently, the corresponding champion inverted PSC exhibited a remarkably high efficiency of 20.1%⁶⁷. Currently, inverted PSCs based on the two-step method have a record PCE of

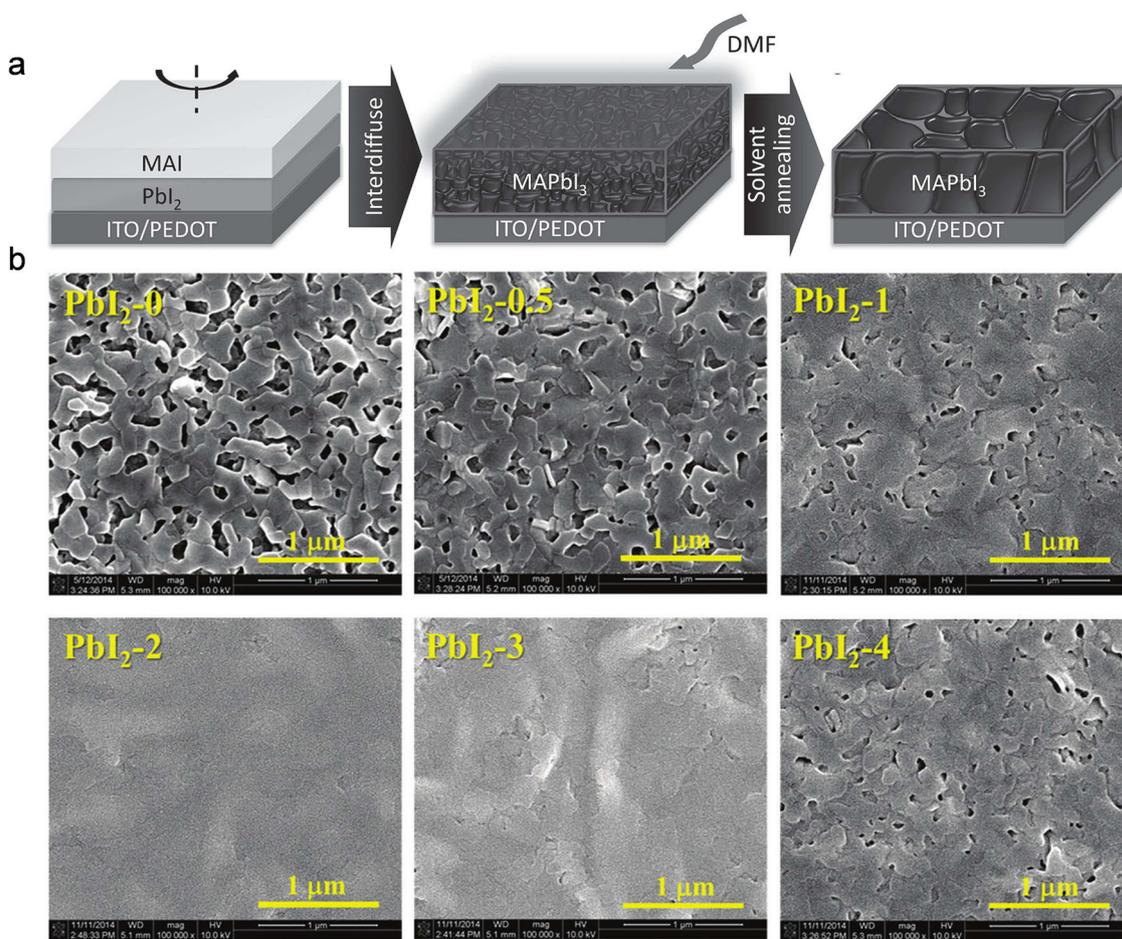


Fig. 3 Two-step solution method fabrication and optimization. **a** Schematic illustration of the interdiffusion in the spin-stacking of double layers of PbI_2 and MAI and solvent annealing process. Reproduced with permission from Ref. ⁶⁵. Copyright 2014, Wiley-VCH. **b** SEM images of PbI_2 films fabricated from PbI_2/DMF solutions with different H_2O contents. Reproduced with permission from Ref. ⁶⁷. Copyright 2015, Royal Society of Chemistry.

22.5%⁶⁸, which is still significantly lower than the best PCE reported for inverted PSCs (a PCE of 25.37%) based on the one-step method¹⁹.

Compared with the two-step method, the one-step method for fabricating perovskite films has become the mainstream method for fabricating high-efficiency inverted PSCs, possibly because (1) the conversion of PbI_2 into perovskite is inefficient in the two-step method, especially when the humidity in the ambient air is hard to control³⁹, and (2) the perovskite films fabricated by the two-step method usually exhibit roughness on the order of tens of nanometers. Although approximately 200 nm spiro-OMeTAD is not sensitive to such a large roughness, such films cannot be well covered by a thin PCBM or C_{60} layer with an approximately 30 nm thickness. The thickness of the PCBM or C_{60} layer seriously affects the photoelectric performance of inverted PSCs. The FF of a PSC decreases sharply with increasing PCBM or C_{60} thickness,

indicating that a thin ETL is critical for reducing series resistance and promoting charge extraction^{36,69,70}. Hence, a flat perovskite surface is crucial for attaining a thin ETL in high-efficiency inverted PSCs. The one-step method meets this demand, which is discussed in the following section.

One-step solution method

Similar to regular PSCs, for inverted PSCs, the one-step solution method is the most widely used perovskite deposition method. In this method, a perovskite precursor solution consisting of metal halide and organic ammonium salt in an appropriate solvent is deposited onto the substrate directly. Generally, the one-step solution method based on spin coating requires an antisolvent extraction step for high-efficiency PSCs. Briefly, antisolvent extraction is a fabrication process whereby an antisolvent is dropped onto a spinning perovskite

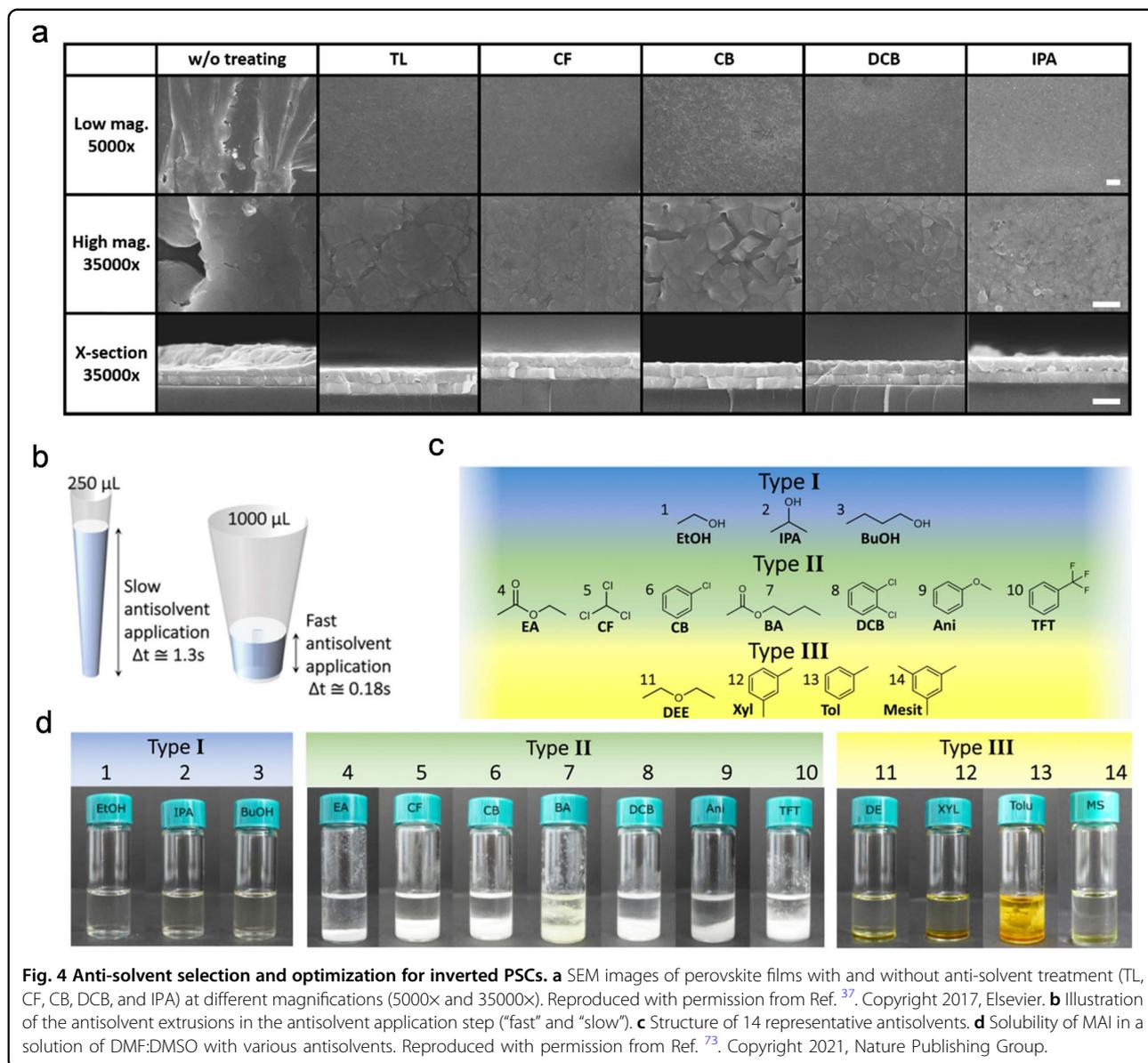
precursor solution prepared by the one-step method to rapidly remove the solvent, which results in the instant growth of perovskites without the formation of any intermediate species⁷¹. The basic function of the antisolvent is to quickly remove excess solvents and quickly create numerous crystal nuclei for forming the ammonium halide-PbI₂-perovskite solvent phase, leading to homogeneous and smooth perovskite films⁷². Note that the antisolvent is a solvent that has good compatibility with the perovskite precursor solvent but poor solubility for the perovskite, such as chlorobenzene (CB), ethyl acetate (EA), and toluene (TL). A suitable antisolvent is crucial to obtaining quality perovskite films. Wu et al. systematically studied the effect of several antisolvents on the morphology of perovskite films, including TL, CB, chloroform (CF), dichlorobenzene (DCB), and isopropyl alcohol (IPA)³⁷. As shown in Fig. 4a, compared with that treated with other antisolvents, the perovskite film treated with TL had a better morphology with large grains since toluene, which has a low dielectric constant, pushed the perovskite precursor into the metastable zone rather than the supersaturation zone (CF, CB, DCB, or IPA) during dropwise addition. In contrast, when the perovskite precursors were treated with other antisolvents (CF, CB, or DCB), the colors of the perovskite layer were brown or light brown, which indicated higher nucleation rates than crystal growth rates during antisolvent treatment, thereby producing smaller grain sizes.

In addition to solvent selection, the duration (Δt) of the application of antisolvent also has an important influence on the morphology of perovskite films⁷³. To investigate the effect of the extrusion rates and duration of the antisolvent application step, Vaynzof et al. prepared perovskite films via 14 different antisolvents by manipulating the antisolvent application rate (Fig. 4b, c)⁷³. They found that the slow or fast application of an antisolvent depends on the solubility of organic iodides in the antisolvent and the miscibility of an antisolvent with perovskite host solvents. As shown in Fig. 4d, Type I antisolvents resulted in a well-mixed and clear solution, indicating that a considerable amount of the organic halides in the DMF:DMSO host solvent was removed by the slow application of antisolvents, leaving higher amounts of PbI₂ on the perovskite surfaces, thereby reducing the perovskite film quality. Type II antisolvents exhibited low solubility for organics. However, they were still miscible with the host solvent, leaving the perovskite films fabricated by Type II antisolvents unaffected by the duration of antisolvent application, as these antisolvents only removed the host solvent while leaving the perovskite composition intact. For Type III antisolvents, liquid phase separation in combination with a yellowish color change was observed, likely caused by the immiscibility of the solvents. There is inadequate time for the host solvent to diffuse across the liquid-liquid interface into the antisolvent when

they are applied quickly, resulting in rough films. Based on the influence of the above antisolvents on device performance and the controlled application rate for each antisolvent, high-quality perovskite films and high-performance inverted PSCs with PCEs over 21% were obtained. To date, the PCE of inverted PSCs based on the one-step solution method with antisolvents has reached an astonishing value of over 25%¹⁹, further narrowing the efficiency gap between inverted PSCs and regular PSCs. In addition to the antisolvent method, gas-assisted treatment, and vacuum flash-assisted processes have also been used to produce high-quality perovskite films based on similar perovskite nucleation and growth mechanisms^{74,75}.

Other methods

The above fabrication methods have been successfully applied for small-area PSCs, which are generally based on spin-coating. However, this approach might not be suitable for scale-up and commercialization due to the centrifugal force required to rapidly remove the solvents (such as DMSO or DMF) while the substrate is rotated at high speed and difficulties in the antisolvent dropping process⁷⁶, which usually leads to poor-quality large-area perovskite films with rough surfaces and pinholes. Hence, the properties of the solvents are crucial because the drying process is expected to be the rate-determining step for the crystallization of the perovskite phase⁷⁷. Therefore, developing precursor solvents and new fabrication methods is key for producing high-quality large-area perovskite films. In this regard, scalable fabrication methods, such as blade and slot-die coating, have emerged and are most widely used for inverted PSCs and modules^{78,79}. However, these fabrication methods for large-area perovskite films also face difficulties, such as in controlling the nucleation and growth rate of perovskite crystals^{77,78}. Rapid crystallization at low temperatures usually leads to undesirable perovskite films with low crystallinity, high defect density, and small grain size, impairing PSC efficiency and stability. A slower and/or higher temperature process is generally employed to grow perovskite films with high crystallinity and large grain sizes⁷⁸. Therefore, a balance between the low crystallinity caused by rapid deposition and the need for high crystallinity with large grains is essential for high efficiency and stable PSCs. To this end, Huang et al. mixed highly volatile 2-methoxyethanol (2-ME) and acetonitrile (ACN) as substitutes for DMF. They mixed them with the low-volatility-coordinating solvent DMSO in a particular proportion to obtain a solution that served as the solvent of the perovskite precursor for blade coating (Fig. 5a)⁷⁸. The coordination ability of the solution/solid mixture with DMSO increased until DMSO was evaporated from the as-coated films because DMSO evaporates much more slowly than other solvents. The rate of solvent



evaporation affects the solid film formation and perovskite crystallization processes in blade coating, resulting in the production of large grain sizes when rapidly drying perovskite films at room temperature (Fig. 5b). Based on this strategy, large-area and uniform perovskite films were successfully obtained at an ultrafast speed of 99 mm s^{-1} and room temperature. This method resulted in an increase in the efficiency of an inverted perovskite solar module by 16% for an aperture area of over 60 cm^2 . In their later research, a steady-state certified efficiency of 19.2% with an aperture area of 50.0 cm^2 was achieved for perovskite modules by blade coating²⁶.

Similar to blade coating, slot-die coating is also widely used to fabricate high-quality large-area MAPbI_3 perovskite films⁸⁰ for perovskite solar modules with

impressive device performance⁸¹. However, the volatile properties and thermal decomposition limit the device's long-term stability⁴³. Hence, it is better to develop modules with FACs perovskites to meet commercialization requirements, due to their excellent thermal stability. However, FACs-based perovskite modules prepared by slot-die coating are rarely reported, which is due to the complexity of the nucleation and crystallization caused by the presence of various halogen ions and the solubility of Cs^+ precursors⁸². To this end, Chen et al. employed a nonvolatile Lewis base additive, diphenyl sulfoxide (DPSO), to form DMF-N-methyl-2-pyrrolidinone (NMP)-DPSO perovskite ink for a FACs perovskite. DPSO was used to enhance the nucleation energy barrier and effectively retard the natural nucleation of perovskite during

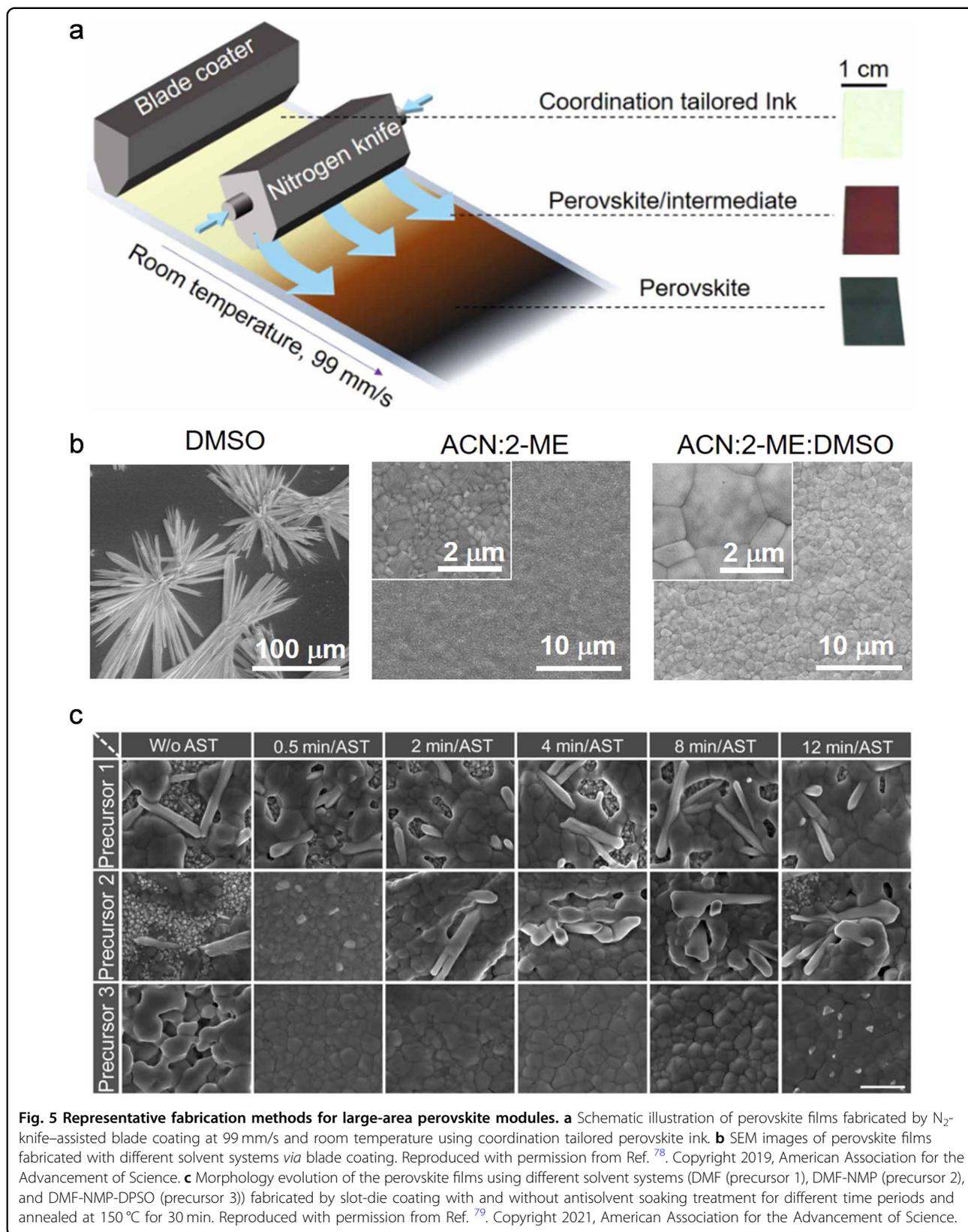


Table 2 Summary of the perovskite composition, module structure, efficiency, and perovskite film deposition method of representative inverted perovskite solar modules (note that perovskite is abbreviated as PVK, and this table only includes data from studies on inverted perovskite solar modules with a total area larger than 10 cm²).

Perovskite	Module structure	Area (cm ²)	PCE (%)	Perovskite film deposition method	References
Cs _{0.05} (FA _{0.9} MA _{0.1}) _{0.95} Pb(I _{0.9} Br _{0.1}) ₃	ITO/NiO _x /PTAA/PVK/PCBM/BCP/Ag	19.16 ^{da}	15.7	Slot-die coating	160
Cs _{0.05} (FA _{0.9} MA _{0.1}) _{0.95} Pb(I _{0.9} Br _{0.1}) ₃	FTO/NiO _x /PTAA/Al ₂ O ₃ /PVK/PEAI/PCBM/BCP/ALD-SnO ₂ /Ag	11.2 ^{ac}	16.9	Spin coating	161
(FA _{0.95} MA _{0.05})Pb(I _{0.95} Br _{0.05}) ₃	ITO/PTAA/PVK/PCBM/BCP/Ag	17.11 ^{ap}	17.8 (certified)	Vacuum Flash-assisted processing	162
MAPbI ₃	ITO/P3HT-COOH/PVK/PCBM/PEI/Ag,	36.6 ^{ac}	16.06	Spin coating	163
MAPbI ₃	ITO/NiO _x /PVK/PCBM/BCP/Ag	25.0 ^{ap}	16.12	Meniscus-coating	164
FA _{0.92} Cs _{0.08} PbI ₃	ITO/PTAA/PVK/C ₆₀ /BCP/Cu	29.5 ^{ap}	18.6 (certified)	Blade coating	165
MA _{0.7} FA _{0.3} PbI ₃	ITO/PTAA/PVK/C ₆₀ /BCP/Cu	63.7 ^{ap}	16.4 (certified)	Blade coating	78
FA _{0.83} Cs _{0.17} PbI _{2.83} Br _{0.17}	FTO/NiMgLiO/PVK/LiF/C ₆₀ /BCP/Bi/Ag	20.77 ^{ac}	16.63 (certified)	Slot-die coating	79
MA _{0.6} FA _{0.4} PbI ₃	ITO/PTAA/PVK/C ₆₀ /BCP/Cu	50.0 ^{ap}	19.2 (certified)	Blade coating	26
Cs _{0.05} (FA _{0.9} MA _{0.1}) _{0.95} Pb(I _{0.9} Br _{0.1}) ₃	ITO/PTAA/Al ₂ O ₃ /PVK/C ₆₀ /SnO ₂ /Ag	12.84 ^{ap}	21.07 (certified)	Spin coating	27

ac active area, ap aperture area, da designated area (active area + dead area for interconnections), P3HT-COOH poly[3-(6-carboxyhexyl) thiophene-2,5-diy], PEI polyethylenimine.

the slot-die coating process to obtain high-coverage wet films. The wet films were immersed in the less toxic antisolvent n-hexane for extraction. Consequently, the DMF-NMP-DPSO precursor produced compact and uniform perovskite films within 8 min (Fig. 5c). The resulting inverted perovskite solar modules achieved a certified quasi-stabilized efficiency of 16.63% with an active area of 20.77 cm². These advancements show that solvent selection is crucial for obtaining quality perovskite modules. Hence, it is imperative to develop perovskite solutions to adjust the nucleation and growth of perovskite crystals to fabricate high-quality large-area perovskite films (>50 cm²) for commercialization. The results of recent studies on representative inverted perovskite solar modules are summarized in Table 2.

Charge transport materials (CTMs)

CTMs (i.e., HTMs and ETMs) determine the separation and transport of carriers in PSCs and have an important impact on device performance. In inverted PSCs, HTMs are often used between the transparent conductive oxide (TCO) and the perovskite layer, while ETMs are generally deposited on the perovskite layer. The basic function of the HTMs (ETMs) is to enhance the extraction rate of photogenerated holes (electrons) and prevent electrons (holes) from transferring from the perovskite conduction band minimum (CBM) (valence band maximum, VBM) to the TCO (CEMs). With proper energy level alignment between the CTMs and a perovskite, photogenerated

carriers can be effectively separated through the built-in electric field at the two interfaces, suppressing non-radiative recombination in inverted PSCs^{29,30}. Therefore, CTMs with excellent photoelectric properties are critical for obtaining efficient and stable inverted PSCs.

HTMs

As “window materials”, HTMs greatly influence the efficiency and stability of inverted PSCs. Generally, HTMs have the following features: i) high optical transmittance to prevent the waste of photon energy in HTMs; ii) suitable energy level structures, that is, the highest occupied molecular orbital (HOMO) energy level of HTMs must be aligned with the VBM of perovskite, which is conducive to reducing interfacial nonradiative recombination; iii) high hole mobility, which reduces the transport resistance of inverted PSCs and seriously affects the device performance; iii) compatibility with perovskite precursors, i.e., they cannot be dissolved by the solvent of perovskite precursors, nor can they interact with the components of perovskite; and iv) suitable film-forming properties, which are conducive to forming high-quality thin films. The HTMs in inverted PSCs can be roughly classified into inorganic and organic HTMs.

Organic HTMs

Organic HTMs are widely used in inverted PSCs because they are suitable for low-temperature solution processes, and their properties can be finely tuned through molecular

design. We classify organic HTMs into polymer HTMs and the burgeoning class of small-molecule HTMs according to their molecular weight.

Common polymer HTMs for inverted PSCs are poly(3,4-ethylenedioxythiophene):poly(styrenesulfonate) (PEDOT:PSS), poly(*N,N'*-bis(4-butylphenyl)-*N,N'*-bis(phenyl)benzidine) (poly-TPD), poly(bis(4-phenyl) (2,4,6-trimethylphenyl) amine (PTAA), etc. However, PEDOT:PSS is faced with the problems of the mismatch between the energy levels of perovskites and the high acidity of the PSS chain^{83,84}. Poly-TPD has the problems of non-wettability and high cost⁸⁵. Inverted PSCs based on these two HTMs have an insufficient efficiency that limits their application in high-efficiency inverted devices.

PTAA also has the disadvantages of non-wettability and high cost, similar to poly-TPD. However, due to its more suitable energy level alignment with the perovskite layer, excellent conductivity, and chemical neutrality with high optical transmittance⁸⁶, it has been successfully applied to improve the efficiency of inverted PSCs. Currently, the efficiency of inverted PSCs based on PTAA has increased beyond 25%^{18,19}. In early studies, most of the literature reported that PTAA showed relatively low hole mobility, which needed to be improved by chemical doping^{87,88}. Among the many dopants used, the most common dopant is 2,3,5,6-tetrafluoro-7,7,8,8-tetracyanoquinodimethane (F4-TCNQ). In 2015, Huang et al. first reported highly efficient solution-processed inverted PSCs using F4-TCNQ-doped PTAA as the HTM⁸⁹, which significantly reduced the series resistance of the PTAA and promoted charge transfer. Consequently, the inverted PSCs had a high efficiency of 17.5% with a V_{OC} of 1.09 V. This report quickly attracted extensive attention. Afterwards, F4-TCNQ was widely used to dope PTAA for high-efficiency inverted PSCs. However, this dopant is very expensive, and the doping additive increases the complexity of the device fabrication process. To this end, Zhang et al. selected PTAA with different molecular weights (MW) to study the surface properties of these PTAA and their different effects on the upper perovskite films⁹⁰. It was found that the performance of PTAA with a molecular weight of 25000 was the best, producing a record efficiency of 18.11% with negligible hysteresis, which indicated that the inverted PSCs based on non-doped PTAA could also exhibit excellent performance.

It should be noted that the surface of PTAA is hydrophobic, making it difficult to obtain continuous and compact perovskite films⁹¹. The pre-wetting method using DMF/DMSO solvents is also beneficial for alleviating the problems caused by the non-wettability of the PTAA surface⁴⁸. However, the effect of this method on improving wettability is not obvious because most DMF/DMSO solvents evaporate quickly during the rapid spin-coating process, leaving only a thin but discontinuous DMF/DMSO layer on PTAA⁹². To this end, Wolf et al. replaced DMSO with NMP

to form a DMF/NMP co-solvent system to enhance the wettability of perovskite precursor inks on PTAA⁹². As shown in Fig. 6a, the binding energy of the MAPbI₃-NMP adduct (−0.728 eV) with PTAA was higher than that of MAPbI₃-DMSO (−0.174 eV) and accompanied by a significant decrease in the contact angle (27.1° versus 50.6°). The improved wettability of perovskite precursor inks on PTAA could inhibit the formation of micro- and nanoscale pinholes, enabling uniform and compact films over large areas. Consequently, the DMF/NMP ink-based inverted devices achieved high PCEs of 21.5% (0.1 cm²) and 19.8% (6.8 cm²), respectively. In addition, incorporating an interlayer is also an effective method for improving the wettability of PTAA^{93,94}. For instance, Gong et al. introduced a novel nondestructive hydrophilic group (C–O and C=O) graft buffer layer (HGGBL) on nonwetable PTAA for perovskite formation by using ozone-treated PMMA-coated PTAA, which decreased the surface potential of PTAA and increased the affinity of the perovskite precursor solution toward PTAA⁹⁴. Furthermore, the C=O bond acted as a Lewis base site to firmly bind PTAA with perovskite crystals. Benefiting from these improvements, the PCEs of inverted PSCs were markedly enhanced from 17.42% to 20.75%.

In addition to the conventional polymer HTMs, other niche polymer-HTMs are also used to fabricate PSCs⁹⁵. Zhu et al. designed a new type of pyridine-based dopant-free polymer HTM (PPY2)⁹⁶, which had better alignment with perovskite energy levels and high hole mobility. Additionally, pyridine effectively passivates uncoordinated Pb²⁺ and iodide defects (Fig. 6b). Based on these advantages, the inverted PSCs using PPY2 as the HTM had an encouraging PCE of up to 22.41% with a high V_{OC} of 1.16 V. Similarly, Wu et al. proposed PTAA-based polymer HTMs fabricated through molecular engineering by removing alkyl groups and adding multifunctional pyridine units⁹⁷. By altering the linking site on pyridine from ortho- (o-PY) to meta- (m-PY) and para- (p-PY) positions, the energy levels and surface wettability were gradually improved. The obvious downfield shift of the proton-signal (from 8.58 to 8.62 ppm) for *m-p* in ¹H NMR measurements suggested that the N-Pb coordination was highly related to the exposure of pyridine-nitrogen with a lone electron pair (Fig. 6c), which was favorable for effectively passivating the interfacial trap states. Ultimately, the optimal p-PY HTM resulted in a remarkably high PCE exceeding 22% (0.105 cm²) and a comparable PCE of over 20% (1 cm²).

Although inverted PSCs using polymer HTMs have achieved great PCEs, the high synthesis cost and hydrophobicity of polymers make the wet chemical deposition of perovskite a great challenge, limiting the application and commercialization of PSCs^{85,98}. On the other hand, small-molecule HTMs have emerged owing to their well-defined molecular mass and structure and photophysical

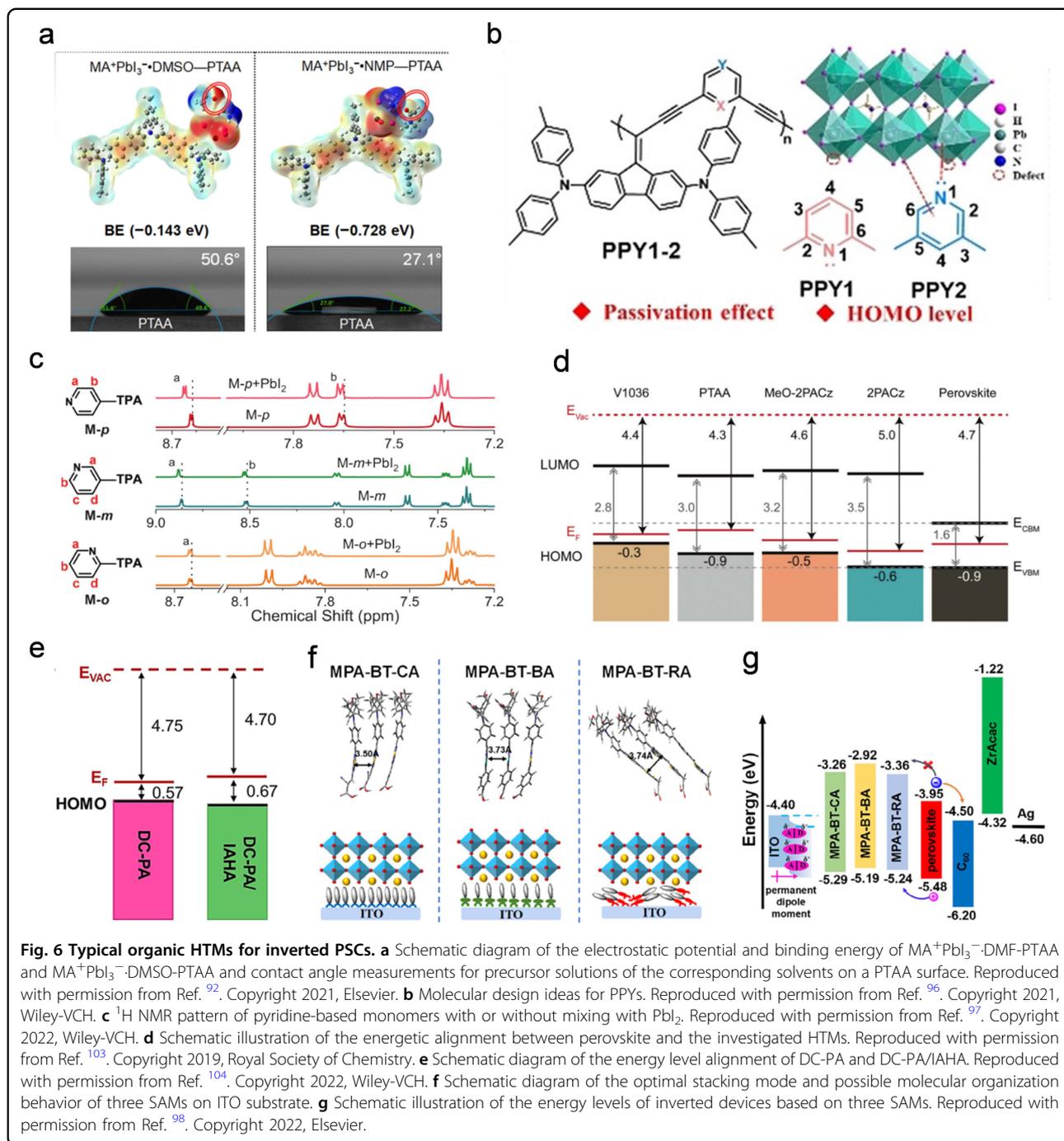


Fig. 6 Typical organic HTMs for inverted PSCs. **a** Schematic diagram of the electrostatic potential and binding energy of $\text{MA}^+\text{PbI}_3^-$ -DMF-PTAA and $\text{MA}^+\text{PbI}_3^-$ -DMSO-PTAA and contact angle measurements for precursor solutions of the corresponding solvents on a PTAA surface. Reproduced with permission from Ref. ⁹². Copyright 2021, Elsevier. **b** Molecular design ideas for PPYs. Reproduced with permission from Ref. ⁹⁶. Copyright 2021, Wiley-VCH. **c** ^1H NMR pattern of pyridine-based monomers with or without mixing with PbI_2 . Reproduced with permission from Ref. ⁹⁷. Copyright 2022, Wiley-VCH. **d** Schematic illustration of the energetic alignment between perovskite and the investigated HTMs. Reproduced with permission from Ref. ¹⁰³. Copyright 2019, Royal Society of Chemistry. **e** Schematic diagram of the energy level alignment of DC-PA and DC-PA/IAHA. Reproduced with permission from Ref. ¹⁰⁴. Copyright 2022, Wiley-VCH. **f** Schematic diagram of the optimal stacking mode and possible molecular organization behavior of three SAMs on ITO substrate. **g** Schematic illustration of the energy levels of inverted devices based on three SAMs. Reproduced with permission from Ref. ⁹⁸. Copyright 2022, Elsevier.

properties⁹⁹. In particular, SAMs provide opportunities for fabricating inexpensive, scalable, and stable HTMs for inverted PSCs due to their low cost, simple synthesis, and relatively easy modification, indicating their promising prospects for application in inverted PSCs and tandem solar cells^{17,100,101}. For example, Getautis et al. designed V1036 as the SAM-HTM of inverted PSCs by simply immersing the substrate in a mixed solution of V1036 and

butylphosphonic acid (C4), which binds to the surface of indium tin oxide (ITO) due to its phosphonic acid anchoring group, and achieved a PCE of 17.8% with an average FF close to 80%¹⁰². In their follow-up study, they designed new generation of SAMs: [2-(3,6-dimethoxy-9H-carbazol-9-yl) ethyl] phosphonic acid (MeO-2PACz) and [2-(9H-carbazol-9-yl)ethyl] phosphonic acid (2PACz)¹⁰³. Compared with V1036, these SAM-based molecules

showed better energy level alignment to the VBM of perovskite (Fig. 6d), which greatly promoted carrier transport at the interface and significantly reduced the interfacial defects. In addition, a good passivation interface was formed due to the chemical compatibility between carbazole and perovskite, thereby suppressing non-radiative recombination. As a result, the champion PCE of the inverted PSCs based on these SAMs exceeded 21%, with a V_{OC} of up to 1.19 V. Afterward, based on previous research, they further designed a new type of SAM, [4-(3,6-dimethyl-9H-carbazol-9-yl)butyl] phosphonic acid (Me-4PACz), and fabricated perovskite/silicon tandem solar cells with a certified efficiency exceeding 29%²¹. Recently, Jen et al. synthesized a new SAM with aligned energy levels and favorable dipole moments, which was based on MeO-2PACz, called ((2,7-dimethoxy-9H-carbazol-9-yl) methyl) phosphonic acid (DC-PA)¹⁰⁴. An alkyl ammonium salt, IAHA, was introduced into the DC-PA solution to form co-SAM. The HOMO energy level of co-SAM was -5.37 eV (Fig. 6e), which is in good alignment with the perovskite energy levels and thus reduced the energy offset. The longer PL lifetime of the co-SAM-based perovskite film suggested suppressed interfacial non-radiative recombination. Benefiting from these advantages, a champion inverted PSC with an excellent PCE of 23.59% and improved device stability was realized.

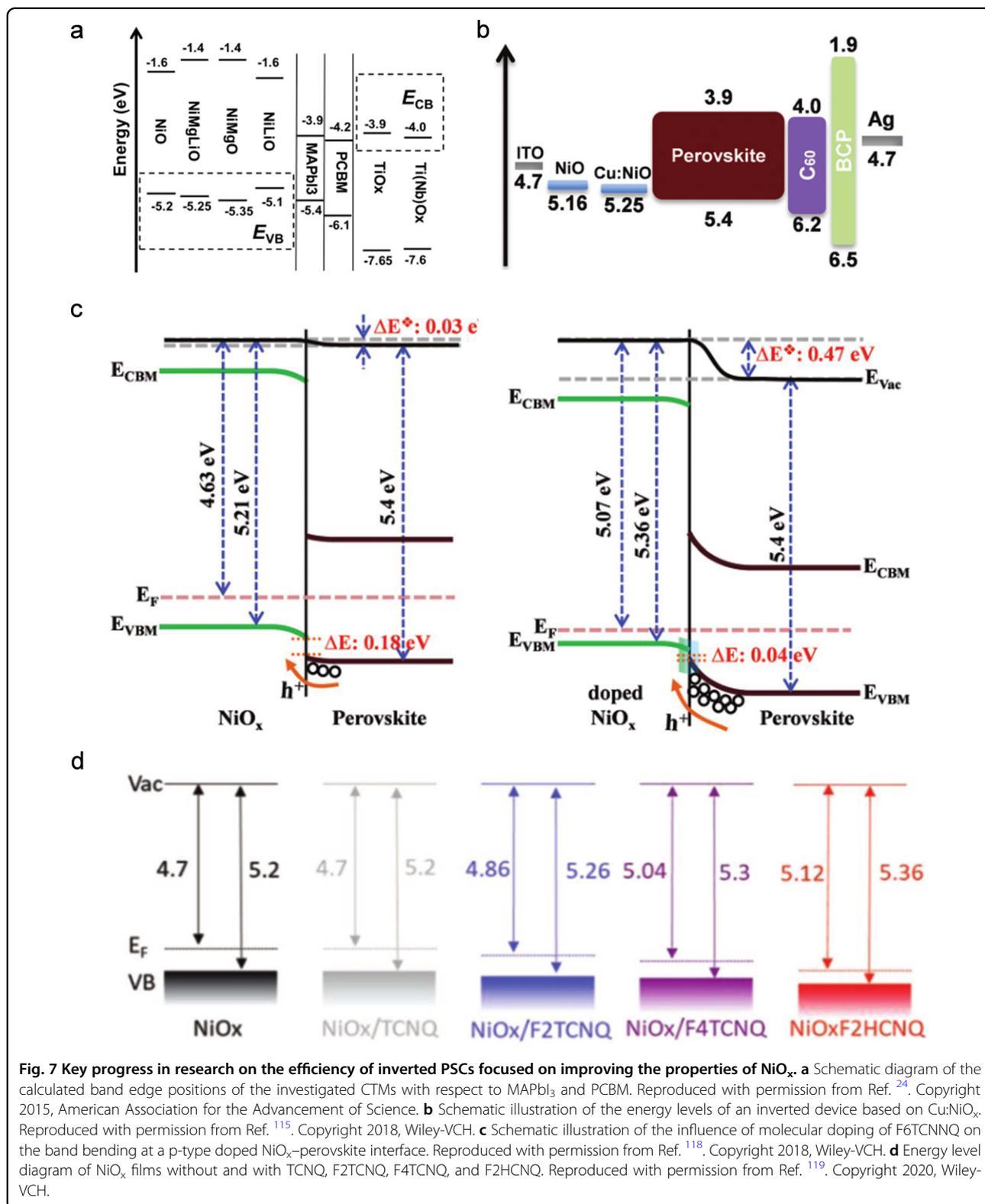
In addition to these SAMs with a carbazole moiety as an electron donor unit, researchers also developed small-molecule HTMs with triphenylamine as an electron donor moiety⁹⁸. Guo et al. synthesized a series of donor-acceptor (D-A)-type SAMs (MPA-BT-CA, MPA-BT-BA, and MPA-BT-RA) as HTMs for inverted PSCs¹⁰⁵. MPA-BT-CA maintained much closer intermolecular stacking (3.50 Å) than the other two SAMs, which was favorable for forming a denser and smoother monolayer film via self-assembly (Fig. 6f), thus allowing high-quality perovskite films to be obtained on the ITO/MPA-BT-CA substrates. In addition, the HOMO energy levels of MPA-BT-CA match better with the energy levels of perovskite (Fig. 6g), which enhanced the internal electrical field and boosted charge extraction. Consequently, the inverted PSCs based on MPA-BT-CA achieved a remarkable PCE of 21.81% with an impressive FF of 82%.

Instead of SAMs, small organic molecules have also been used as high-performance HTMs^{98,106,107}. Nevertheless, among small-organic-molecule HTMs, SAM-HTMs are more commonly used because SAMs can allow better interfacial energy level tuning and interface recombination suppression, which greatly improves device efficiency and stability. In particular, SAMs are employed as the HTMs for perovskite/silicon tandem devices and inverted PSCs with the highest efficiency^{19,21}. For mainstream polymer HTMs, PTAA is commonly used in high-efficiency inverted PSCs^{18,25,108}. However, its non-

wettable surface and high cost seriously limit its commercial application. Compared with PTAA, small organic molecules with comparable performance have the advantages of simple synthesis and low cost. In addition, SAMs are also outstanding when used in tandem solar cells, which may be the main future development direction of perovskite photovoltaics. Hence, SAMs need to be further developed to improve the efficiency of inverted PSCs to rival that of regular PSCs³. In short, the vigorous development of organic HTMs has greatly promoted the efficiency and stability of inverted PSCs.

Inorganic HTMs

Due to their hydrophobicity, high cost of raw materials, and potential degradation, organic HTMs for inverted PSCs also face challenges, which limits the application and commercialization of inverted PSCs. In contrast, inorganic HTMs have attracted much attention due to their excellent long-term stability and thermal stability^{109–111}. Among inorganic HTMs, nickel oxide (NiO_x)-based metal oxides are the most successful in inverted PSCs and have been widely investigated due to their favorable energy level alignment with most perovskite absorbers and excellent stability as well as facile synthesis and deposition¹¹². Generally, stoichiometric NiO is insulating; therefore, the conductivity of NiO_x depends heavily on the intrinsic Ni vacancies (or self-doping of Ni^{3+}), which increases the series resistance of devices and requires strict thickness manipulation. However, the hole charge density of undoped NiO_x is seriously affected due to the large ionization energy of Ni vacancies, resulting in comparatively low conductivity. To this end, metal cations, such as Ag^+ , Au^+ , Cu^{2+} , Cs^+ , K^+ , and certain molecules were doped into NiO_x to improve its conductivity and adjust its energy level by tuning the concentration of Ni vacancies^{113–117}. Han et al. developed a heavily p-doped (p^+) $\text{Ni}_x\text{Mg}_y\text{Li}_{1-x-y}\text{O}$ codoping strategy in which 15 mol% Mg^{2+} was doped in 5 mol% Li^+ -doped NiO_x to compensate for the unfavorable positive shift of its VBM caused by Li^+ doping into the NiO_x lattice (Fig. 7a)²⁴. Accordingly, the conductivity of the $\text{Li}_{0.05}\text{Mg}_{0.15}\text{Ni}_{0.8}\text{O}$ film was $2.32 \times 10^{-3} \text{ S cm}^{-1}$, which was approximately 12 times greater than that of the undoped sample, indicating the notable reduction in the series resistance and increase in the shunt resistance, which is advantageous for manufacturing large-area ($>1 \text{ cm}^2$) PSCs. As a result, a large-area ($>1 \text{ cm}^2$) PSC with a high PCE of 16.2% (certified 15%), which was the world record efficiency of large-area ($>1 \text{ cm}^2$) PSCs at that time, was obtained. Later, He et al. developed copper-doped NiO_x (Cu:NiO) nanoparticle inks at room temperature (RT) without further processing based on previous work¹¹⁵. Cu^+ and Cu^{2+} states were observed for the Cu:NiO film. The conductivity of the NiO_x film was improved due to the substitution of Cu^+ for Ni^{2+} , which improved the hole mobility. In addition, the VBM of the Cu:NiO film



underwent a favorable negative shift (Fig. 7b), leading to improved charge transfer and extraction at the buried interface. Consequently, a PCE of up to 20.15% was achieved

for the corresponding inverted PSCs. Similarly, He et al. proposed a molecule-doped NiO_x that involved a strong electron acceptor, 2,2'-(perfluoronaphthalene-2,6-diylidene)

dimalononitrile (F6TCNNQ), with a low lowest unoccupied molecular orbital (LUMO, -5.37 eV)¹¹⁸. The E_F of the doped NiO_x increased from -4.63 to -5.07 eV and decreased the energy level offset between the VBM of NiO_x and the perovskite absorber from 0.18 to 0.04 eV (Fig. 7c), which greatly enhanced hole extraction and reduced interfacial nonradiative recombination. As a result, the best PCE of inverted PSCs based on NiO_x was as high as 20.86%. Inspired by this method, Chen et al. systematically investigated the effect of doping several molecules with high electron affinity similar to that of F6TCNNQ, including 3,6-difluoro-2,5,7,7,8,8-hexacyanoquinodimethane (F2HCNQ), F4TCNQ, TCNQ and 2,5-difluoro-TCNQ (F2TCNQ), into NiO_x ¹¹⁹. F2HCNQ exhibited the highest electron affinity (EA), which enhanced the charge transfer from the VBM of NiO_x to the LUMO of the molecules. The increased W_F and VB resulting from the high EA resulted in more suitable energy level alignment at the NiO_x /perovskite interfaces (Fig. 7d), leading to fast interfacial hole extraction with lower energy loss. Consequently, the efficiency of inverted PSCs based on F2HCNQ- NiO_x fabricated by a low-temperature process exceeded 22% for the first time.

Even though inverted PSCs based on NiO_x have yielded great results, their record PCEs are still lower than those of PTAA- or SAM-based PSCs, which can be attributed to the following reasons: (1) abundant surface defects and energy level mismatch result in large energy offset at the NiO_x /perovskite interface¹¹², which significantly aggravates interfacial carrier recombination, thereby impeding charge carrier extraction; (2) high-oxidative-state Ni^{3+} can react with A-site cation salts to form $\text{PbI}_{2-x}\text{Br}_x$, resulting in the formation of A-site defects and $\text{PbI}_{2-x}\text{Br}_x$ -rich perovskite at the NiO_x /perovskite interface¹²⁰, which results in a hole extraction barrier and noncapacitive hysteresis; and (3) light-induced deprotonation at the NiO_x /perovskite interface generates interfacial voids/vacancies and causes the formation of shallow-level defects and strong ion movement, thus leading to inferior efficiency^{121,122}. The inverted PSCs based on NiO_x , which is the most promising inorganic HTM, have yielded great results, with a certified PCE of 23.91%¹⁷. Many efforts have been made to improve the efficiency and stability of inverted PSCs based on NiO_x , which is discussed later.

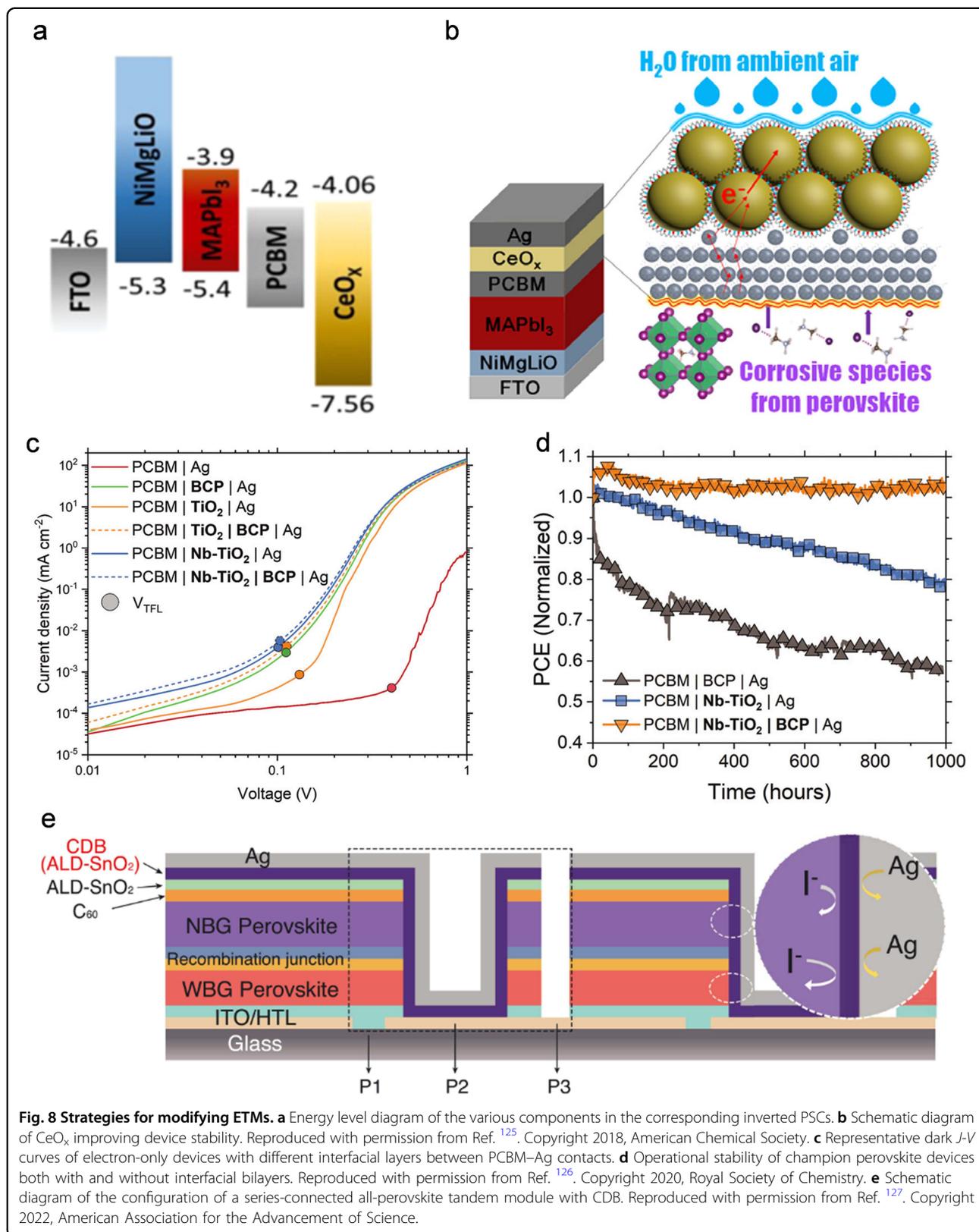
ETMs

As materials for electron selective contact, the ETMs on top of perovskite films play an important role in high-efficiency inverted PSCs. Well-known star ETMs, fullerenes, and their derivatives (PCBM and C_{60}) have been extensively used in high-efficiency inverted PSCs due to their high electron mobility and low-temperature processing^{17–19}. Therefore, research on ETMs is more focused on finding inorganic alternatives for double-layer ETMs to improve the efficiency and stability of inverted PSCs due to

their superior intrinsic stability to improve PCE and stability at lower cost^{123,124}. In this regard, Chen et al. introduced low-cost cerium oxide (CeO_x) nanocrystals as an inorganic ETM¹²⁵, which exhibited promising high electron mobility ($10^3 \text{ cm}^2 \text{ kV}^{-1} \text{ s}^{-1}$) and suitable energy level alignment for efficient charge extraction (Fig. 8a). Consequently, inverted PSCs with the configuration of $\text{NiMgLiO}/\text{MAPbI}_3/\text{PCBM}/\text{CeO}_x$ achieved a high efficiency of 18.7%. The resulting PSCs also showed excellent stability, maintaining 91% of their initial PCEs when kept in air with controlled humidity ($\sim 30\%$) under continuous light immersion, due to the special chemical shielding effect of the PCBM/ CeO_x bilayer ETL. This configuration could prevent ambient moisture from corroding the perovskite and prevent perovskite species from corroding the Ag electrode (Fig. 8b). Similarly, Troughton et al. used PCBM/Nb-doped TiO_2 as a multi-layer ETM, which greatly improved the ohmic response of the corresponding device with a structure of PCBM-Nb- TiO_2 - bathocuproine (BCP)-Ag, indicated by the dramatically reduced V_{TFL} (Fig. 8c)¹²⁶, thereby enhancing the electron mobility of the reference ETM. As a consequence, the PCE of inverted PSCs was enhanced from 18.7% to 20.7% with up to 83% FF, without any degradation for at least 1000 h under continuous light immersion in a nitrogen atmosphere (Fig. 8d). Even with great success, the performance of the highest-efficiency inverted PSCs based on either inorganic ETM alone or fullerene/inorganic ETMs as selective electron contacts still lags behind that of organic ETM-based PSCs.

Moreover, atomic-layer-deposited SnO_2 (ALD- SnO_2) has recently attracted increasing attention due to the increased popularity of perovskite tandem devices^{21,22,127}. In this regard, SnO_2 is usually deposited on the ETM as a buffer layer. For example, SnO_2 is often used as a buffer layer in perovskite/silicon tandem devices to reduce the damage to perovskite caused by sputtering ITO²¹. In all-perovskite tandem solar cells, ALD- SnO_2 is usually used to protect the front cells from the corrosion of PEDOT:PSS²². Recently, Tan et al. proposed a thin conformal diffusion barrier (CDB)¹²⁷, which consisted of ALD- SnO_2 deposited after P_2 scribing, for inverted tandem modules (Fig. 8e). Here, the electrically conductive CDB acted as not only an electron extractor but also a lateral diffusion barrier between interconnecting subcells to overcome halide-metal interdiffusion, and the reaction between the perovskites and metal electrodes was prevented. Due to these benefits, a certified PCE of 21.7% with an aperture area of 20.25 cm^2 was achieved for the corresponding all-perovskite tandem solar modules. These modules also showed excellent stability, retaining 75% of their initial efficiency after 500 h of continuous operation under simulated one-sun illumination.

Overall, the ETMs used in high-efficiency inverted PSCs are still PCBM or C_{60} . Inorganic layers can be used as



double-layer ETMs based on fullerene/inorganic metal oxide to improve the stability of inverted PSCs. However, the high costs of fullerenes and their derivatives (PCBM

and C_{60}) limit their commercialization. Therefore, more research is needed to obtain better ETMs to improve the efficiency and stability of inverted PSCs.

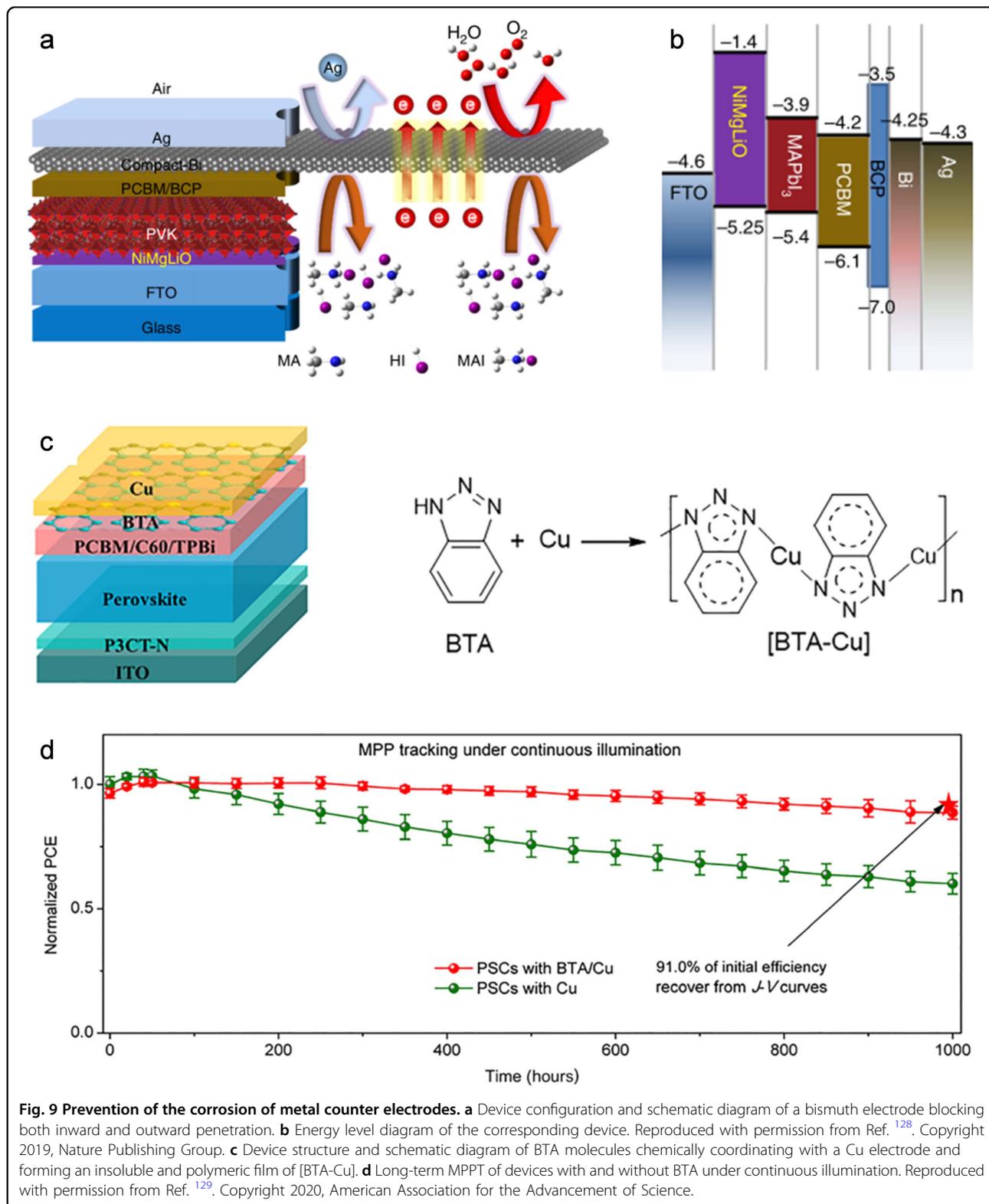


Fig. 9 Prevention of the corrosion of metal counter electrodes. **a** Device configuration and schematic diagram of a bismuth electrode blocking both inward and outward penetration. **b** Energy level diagram of the corresponding device. Reproduced with permission from Ref. ¹²⁸. Copyright 2019, Nature Publishing Group. **c** Device structure and schematic diagram of BTA molecules chemically coordinating with a Cu electrode and forming an insoluble and polymeric film of [BTA-Cu]. **d** Long-term MPPT of devices with and without BTA under continuous illumination. Reproduced with permission from Ref. ¹²⁹. Copyright 2020, American Association for the Advancement of Science.

CEMs

Similar to other interface functional materials, suitable CEMs atop the perovskite layer are also crucial for achieving efficient and stable inverted PSCs. In inverted PSCs, CEMs are generally deposited on thin buffer layers (BCP or 1,3,5-Tris(1-phenyl-1H-benzimidazol-2-yl)benzene (TPBi))^{128,129} on ETMs, which can usually reflect incident light and have an appropriate work function, high conductivity, and good stability, and have a profound impact on the efficiency and stability of PSCs. In this regard, BCP is often used as an interfacial layer in inverted devices, which generally can reduce the Schottky barrier between metal CEMs and commonly used fullerene ETMs due to the tendency of BCP to chelate with metal CEMs, allowing closer electronic contact between fullerene ETMs and metal CEMs, thus promoting interfacial ohmic contact¹²⁶, which is critical for proper electron transport and carrier collection in inverted PSCs. Moreover, the hydrophobic BCP can also prevent erosion by external moisture¹³⁰ and prevent the corrosive problems caused by ion diffusion¹³¹, thus improving the stability of the corresponding devices. Unfortunately, there is a consensus that the metal electrodes (Cu, Ag, Al) commonly used in inverted PSCs undergo corrosion reactions with the decomposition of perovskites during aging^{128–131}. Furthermore, ion migration induced by degradation factors (moisture, heat, and light) also causes active metal counter electrode corrosion, seriously impairing PSC efficiency and stability. In addition, the difference in E_F between ETMs and CEMs causes serious interface charge accumulation and affects charge transfer and collection.

To this end, Chen et al. introduced a chemically inert bismuth (Bi) interlayer into inverted PSCs with the structure of fluorine doped tin oxide (FTO)/NiMgLiO/perovskite /PCBM/BCP/Bi/Ag¹²⁸. In their devices, Bi served as a blocking layer to effectively protect the perovskite from intrusion by undesirable external moisture and protect the Ag electrode from iodine corrosion (Fig. 9a). Moreover, the Bi interlayer with an optimized thickness exhibited a well-matched energy level along with good conductivity, which negligibly affected the transport and collection of electrons in the corresponding devices (Fig. 9b). As a consequence, these devices based on the Bi-interlayer maintained 88% of their initial efficiency in ambient air in the dark for over 6000 h without any encapsulation, and the initial efficiency of these devices was only reduced by 5% after thermal aging at 85 °C in a nitrogen atmosphere for 500 h. In addition, Fang et al. proposed a chemical anti-corrosion strategy by inserting an organic preservative of benzotriazole (BTA) before Cu electrode deposition¹²⁹. In this strategy, the BTA layer did not act as a physical barrier layer as Bi mentioned above but formed an insoluble and polymeric film of [BTA-Cu] through chemical interaction with the

Cu electrode (Fig. 9c). Compared with the reference, the BTA interlayer could act as a diffusion barrier and effectively block Cu or I diffusion with almost no iodine aggregation or Cu diffusion in PSCs with BTA/Cu film during 85 °C aging in a glove box. Benefiting from the above advantages, the device stability was significantly improved. PSCs with BTA maintained over 90% initial efficiency after aging for 1100 h at 85 °C. In addition, the operational stability of PSCs with BTA was also outstanding, maintaining 91% of their initial efficiency under MPPT for 1000 h (Fig. 9d).

Therefore, robust interfacial barriers not only prevent the corrosion reaction of metal electrodes caused by ion migration but also block the diffusion of metal ions toward the perovskite layer, which is essential for achieving high efficiency and stable inverted PSCs. Consequently, in addition to selecting the appropriate metal electrode, the tailored modification of the top electrode is also crucial for obtaining stable devices. To date, various organic and inorganic materials have been employed as interfacial barriers between CTMs and metal electrodes, such as a naphthalene diimide derivative (NDI-BN)¹³², an amine-mediated metal oxide (AM-TiO_x)¹³³, a metal acetylacetonate (ZrAcac)¹³⁴, and poly(methyl methacrylate) (PMMA)¹³⁵. Furthermore, transparent electrodes with excellent optical transmittance are also extensively used for tandem or semitransparent solar cells, including silver nanowires (AgNWs)¹³⁶, indium zinc oxide (IZO)¹³⁷, and ITO¹³⁸. While TCO usually requires a buffer layer (MoO_x, etc.) to protect the HTM/ETM or perovskite layer from damage caused by magnetron sputtering of the TCO counter electrode, there are many inorganic ETL barriers, such as ALD-aluminum-doped zinc oxide (AZO), ALD-SnO_x layers, ALD-TiO₂, and ALD-VO_x, that have also been employed by deposition on top of PCBM/BCP ETLs/buffer layers to provide better protection of the perovskite layer against attack^{139–141}. Overall, the development of a suitable counter electrode strategy is still significantly challenging and requires more effort to achieve efficient and stable inverted PSCs.

Additive and interface engineering

With the continuous optimization of the fabrication methods of perovskite films and the substantial progress in interfacial CTM research, the efficiency and stability of inverted PSCs are increasing. Even with this improvement, their efficiency and stability are still affected by significant nonradiative recombination loss, which leads to serious thermal potential loss and significantly impacts the V_{OC} and FF of devices, thereby limiting device performance. Researchers have recently developed an abundance of methods for reducing defects, suppressing nonradiative recombination, and enhancing device efficiency and stability. Among them, additive engineering and interface

engineering methods for perovskites have attracted extensive attention and are especially popular for high-efficiency inverted PSCs. Herein, the latest research progress in additive engineering and interface engineering for high-efficiency inverted PSCs is summarized.

Additive engineering

Additives are mainly introduced during the fabrication process of perovskite layers to improve the quality of the perovskite films, reduce defects and enhance the stability of devices^{142,143}. Bao et al. used the natural additive capsaicin to completely transform a MAPbI₃ surface region from p-type to n-type during defect passivation¹⁴⁴. It was proven by cross-sectional atomic force microscopy (AFM)-Kelvin probe force microscopy (KPFM) measurements that the p-n homojunction was located 100 nm below the perovskite surface. The E_F of the VBM positively shifted from 0.55 to 1.03 eV, which meant that the energetics of the perovskite surface underwent a complete transition from p-type to n-type. This energetic transformation promoted interfacial charge transport between the perovskite and PCBM, reducing interfacial carrier recombination (Fig. 10a). As a result, an impressive efficiency of 21.88% with a remarkable FF of 83.81% and excellent stability were achieved for the corresponding inverted PSCs. Almost at the same time, a multifunctional sulfobetaine-based zwitterionic surfactant, tetradecyldimethyl(3-sulfopropyl) ammonium hydroxide inner salt (TAH), was incorporated into MAPbI₃ to generate a large-scale coating¹⁴⁵, which not only improved the adhesion of the perovskite ink to the underlying hydrophobic PTAA layer but also accurately tuned the perovskite crystallization kinetics (Fig. 10b). Benefiting from these advantages, a dense and smooth perovskite film with better crystallinity was obtained on the PTAA substrate. In addition, the functionalized zwitterionic groups of TAH could passivate the positively and negatively charged defects at the perovskite surface and grain boundaries (GBs), forming a hydrophobic surface on the upper surface of the perovskite. Consequently, the efficiency of TAH-based inverted PSCs with an active area of 0.04 cm² was increased from 19.34% to 22.07% by blade coating. The resulting PSC also showed superior moisture stability and could maintain 96.7% of its initial PCE after 1200 h in ambient air (25 ± 5 °C and 20 ± 5% relative humidity (RH)).

Furthermore, organic ammonium ($-NH_3^+$) cations have been widely used as passivating layers to improve the efficiency and stability of inverted PSCs¹⁷. For instance, Sargent et al. introduced several surface-anchoring alkylammonium ligands (AALs: BA, PEA, OA, and OAm) with different chain lengths into perovskite precursors as passivating agents²⁵. It was found that the perovskite surface was composed of densely packed alkyl ligands after AALs were anchored on the perovskite matrix, which was

stabilized by van der Waals interactions between the organic moieties of the alkyl ligands. These interactions increased with the alkyl chain length (Fig. 10c). Consequently, long-chain AALs enhanced the crystallinity of perovskite films by regulating the crystal growth orientation and reducing the nonradiative recombination because the long-chain AAL layer could effectively block holes between the perovskite and C₆₀ interfaces. The resulting PSCs with AALs (OAm) achieved a high PCE of 23.0% ($J_{SC} = 24.1 \text{ mA cm}^{-2}$, $V_{OC} = 1.17 \text{ V}$, FF = 81.6%) with a certified stabilized PCE of 22.3% and showed excellent stability with no efficiency loss after 1000 h under MPPT and simulated AM1.5 G illumination. In a later study, they proposed the strategy of mixing the perovskite precursor with large organic cations, i.e., n-butylammonium (BA), ethylammonium (EA), dimethylammonium (DMA), or guanidinium (GUA), to spontaneously form a two-dimensional (2D) passivation layer at the buried interface⁵². EA, DMA, or BA could not form the 2D phase at the perovskite/NiO_x interface. Only GUA could form the 2D GUA₂PbI₄ phase at the buried interface due to its symmetric structure and abundant $-NH_2$ groups. The 2D phase formation was attributed to the hydrogen bonding between the $-NH_2$ groups in GUA and the uncoordinated oxygens in NiO_x, serving as nuclei for growth, thereby passivating the otherwise Ni-deficient NiO_x surface. Consequently, this strategy reduced the defects at the buried interface and suppressed interfacial nonradiative recombination, thus leading to NiO_x-based inverted PSCs with a record PCE of 22.9%. However, these organic monoammonium ligands tended to form undesired in-plane favored 2D structures, which impaired the stability of the device^{146,147}. Therefore, Chen et al. introduced alkyldiammonium salts (1,6-hexamethylenediamine dihydride (HDAI₂), 1,3-propanediamine dihydride (PDAI₂), and 1,4-butanediamine dihydride (BDAI₂)) with different alkyl chain lengths as additives into perovskite precursors¹⁴⁸. Based on density functional theory (DFT) calculations, the BDA ligand had the maximum adsorption energy for V_{FA} compared with the other two ligands due to the bicephalous ammonium groups of BDA interacting with the two V_{FA} sites (Fig. 10d), which was favorable for reducing the defect density and improving the energy level structure of the upper surface of perovskite. Consequently, the inverted PSCs with BDAI₂ achieved high efficiencies of 23.1% and 20.9%, respectively, on the rigid and flexible substrates and retained 92% of the initial efficiency under MPPT for 1000 h.

In addition to the additives mentioned above, polymer additives are widely used in inverted PSCs^{149,150}. However, due to the multifunctional nature of some additives and limited experimental technologies, a complete understanding of the passivation mechanisms for additive engineering has yet to be attained entirely. Therefore, it is

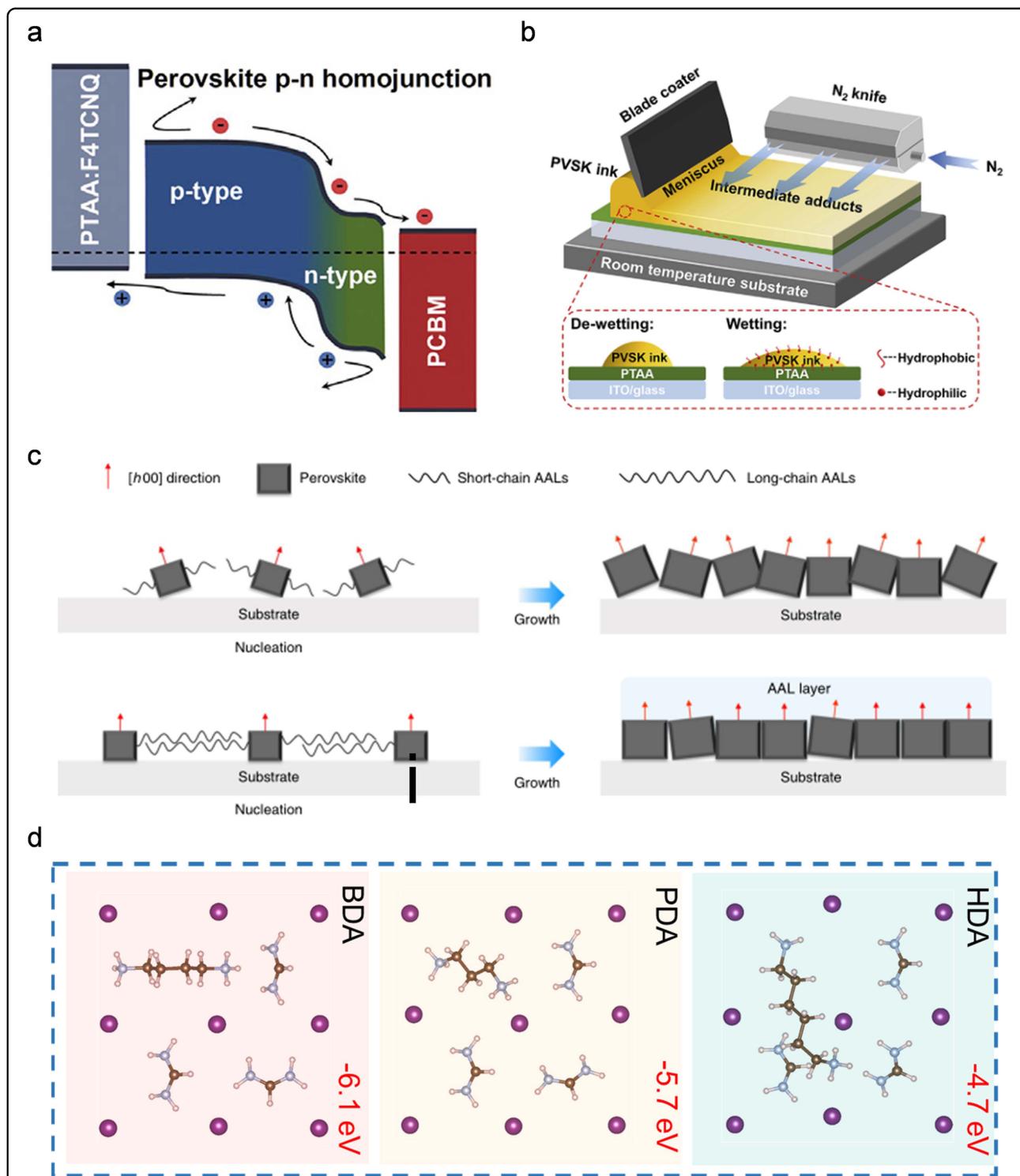


Fig. 10 Additive engineering for improving the photovoltaic performance of inverted PSCs. **a** Energy level bending diagram of perovskite containing capsaicin with respect to CTMs. Reproduced with permission from Ref. ¹⁴⁴. Copyright 2021, Elsevier. **b** Schematic illustration of TAH improving the adhesion of perovskite ink to the underlying hydrophobic PTAA during meniscus coating at room temperature. Reproduced with permission from Ref. ¹⁴⁵. Copyright 2020, Elsevier. **c** Schematic illustration of the influence of short-chain AALs and long-chain AALs on crystallization during perovskite growth. Reproduced with permission from Ref. ²⁵. Copyright 2020, Nature Publishing Group. **d** Theoretical models of the adsorption of three alkyldiammonium ligands (HDA, PDA, and BDA) onto V_{FA} on the perovskite surface. Reproduced with permission from Ref. ¹⁴⁸. Copyright 2022, Wiley-VCH.

necessary to understand the additive passivation mechanism to guide the design and further improve the efficiency and stability of inverted PSCs.

Interface engineering

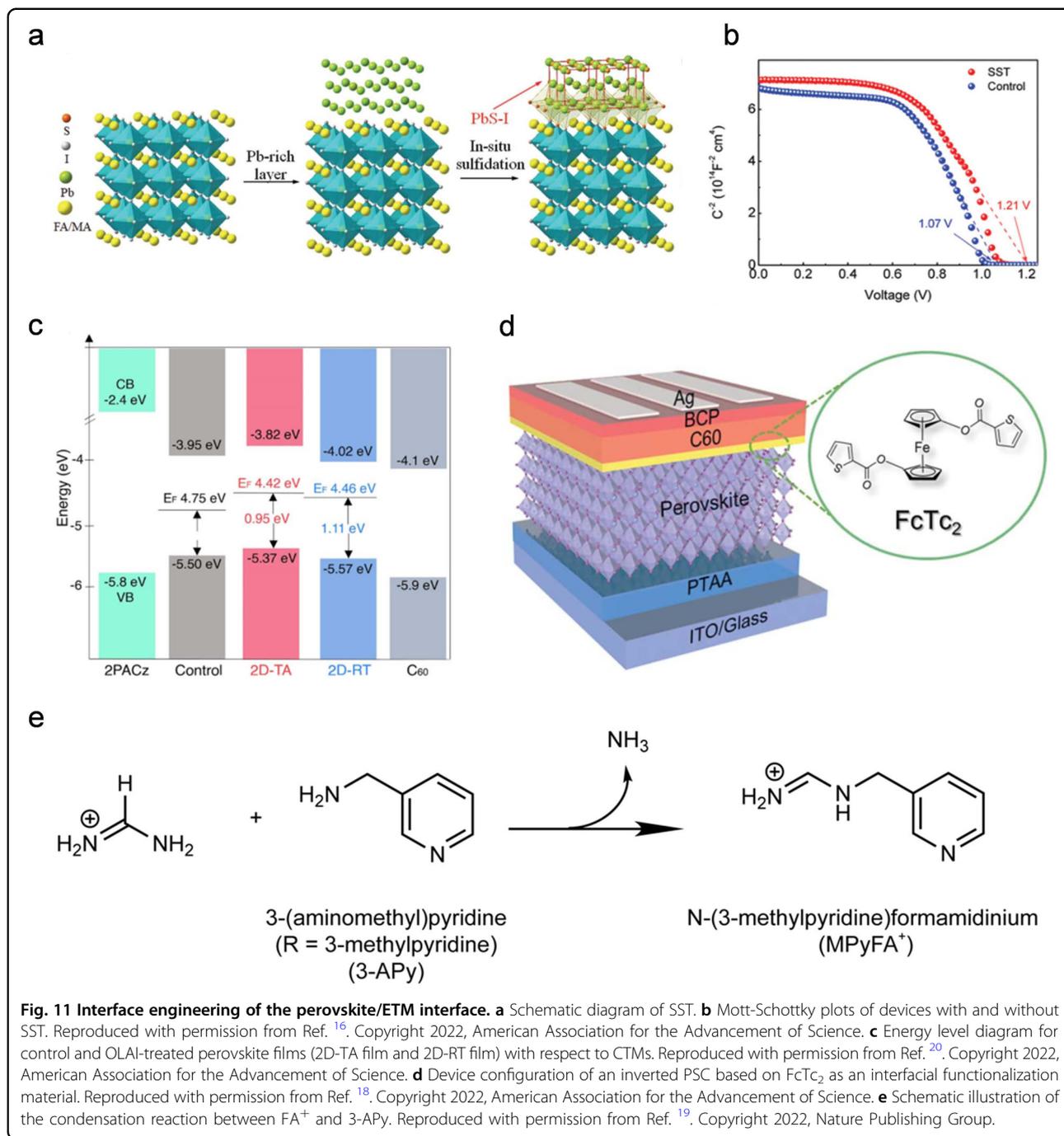
Note that there is still a significant gap in efficiency between inverted PSCs and regular PSCs, which could undermine efforts to adopt the p-i-n architecture, despite the other advantages of inverted PSCs. Given the remarkable advances in perovskite bulk material optimization over the past decade, interface engineering methods have become the most important strategies for pushing PSC performance to its limit. Notably, extraordinary achievements have been made in interface engineering with regard to enhancing the performance of inverted PSCs, as shown in Fig. 2. Compared with shallow-level defects, deep-level defects located in the mid-gap are prone to forming nonradiative carrier recombination centers at the interfaces, causing V_{OC} loss in PSCs. Therefore, low charge recombination at interfaces is critical for enhancing the performance of PSCs. The interface between the perovskite film and the selective top ETM in inverted PSCs is a major issue that induces more interfacial recombination than in perovskite/spiro-OMeTAD regular PSCs, which could be one reason why the efficiency of inverted PSCs is commonly lower than that of regular PSCs^{29,30}. Hence, various studies have been performed to optimize perovskite/ C_{60} interface properties, and interface engineering methods were used as an effective route for tuning the properties of interfaces to overcome interfacial losses without destroying the properties of bulk layers.

Fang et al. proposed surface sulfidation to reduce nonradiative recombination at the interface between perovskite and ETMs to narrow the difference in efficiency between inverted PSCs and regular PSCs. Inverted PSCs were treated (SST) through the surface sulfidation of lead (Pb)-rich perovskite films¹⁶. Specifically, pyridine-2-carboxylic lead (PbPyA₂) was first spin-coated on the perovskite layer to form a Pb-rich perovskite surface, and then hexamethyldisilathiane (TMS) was spin-coated on top by reacting with solid-phase PbPyA₂ (Fig. 11a). The perovskite surface became more n-type with SST, which made the perovskite surface energy band bend and induced an extra back-surface field. This field enhanced the V_{bi} of the device and promoted carrier transport (Fig. 11b). In addition, the Pb-S bonds, formed through the strong interactions between S^{2-} anions and Pb ions on the perovskite surface, were more stable than the Pb-I bonds. Based on the advantages of SST, the certified efficiency of inverted PSCs exceeded 23% for the first time. The resulting devices also showed excellent thermal stability and operational stability and maintained 91.8% of their initial efficiency after thermal aging at 85 °C for

2200 h. Likewise, Wolf et al. constructed tailored-dimensionality 2D/3D heterojunctions on perovskite surfaces at RT using oleylammonium iodide (OLAI). They tailored the dimensionality (n) of the 2D perovskite fragments at the perovskite/ C_{60} interface of inverted PSCs by tuning the annealing conditions from lower to higher temperatures, which are crucial for efficient top-contact passivation through 2D perovskite passivation layers. It was found that the low-dimensional perovskite layers ($n = 1, 2$) became more prominent and had a highly oriented lateral direction on the top 3D-perovskite layers when posttreatment with OLAI was conducted at room temperature (2D-RT), which moved the VBM of 2D-RT films closer to the CBM of C_{60} , thus improving the energy level matching between perovskite and C_{60} and promoting electron transport (Fig. 11c)²⁰. As a result, the inverted PSCs with 2D passivation had a high efficiency of 24.3% and maintained >95% of their initial efficiency under damp-heat test conditions for >1000 h.

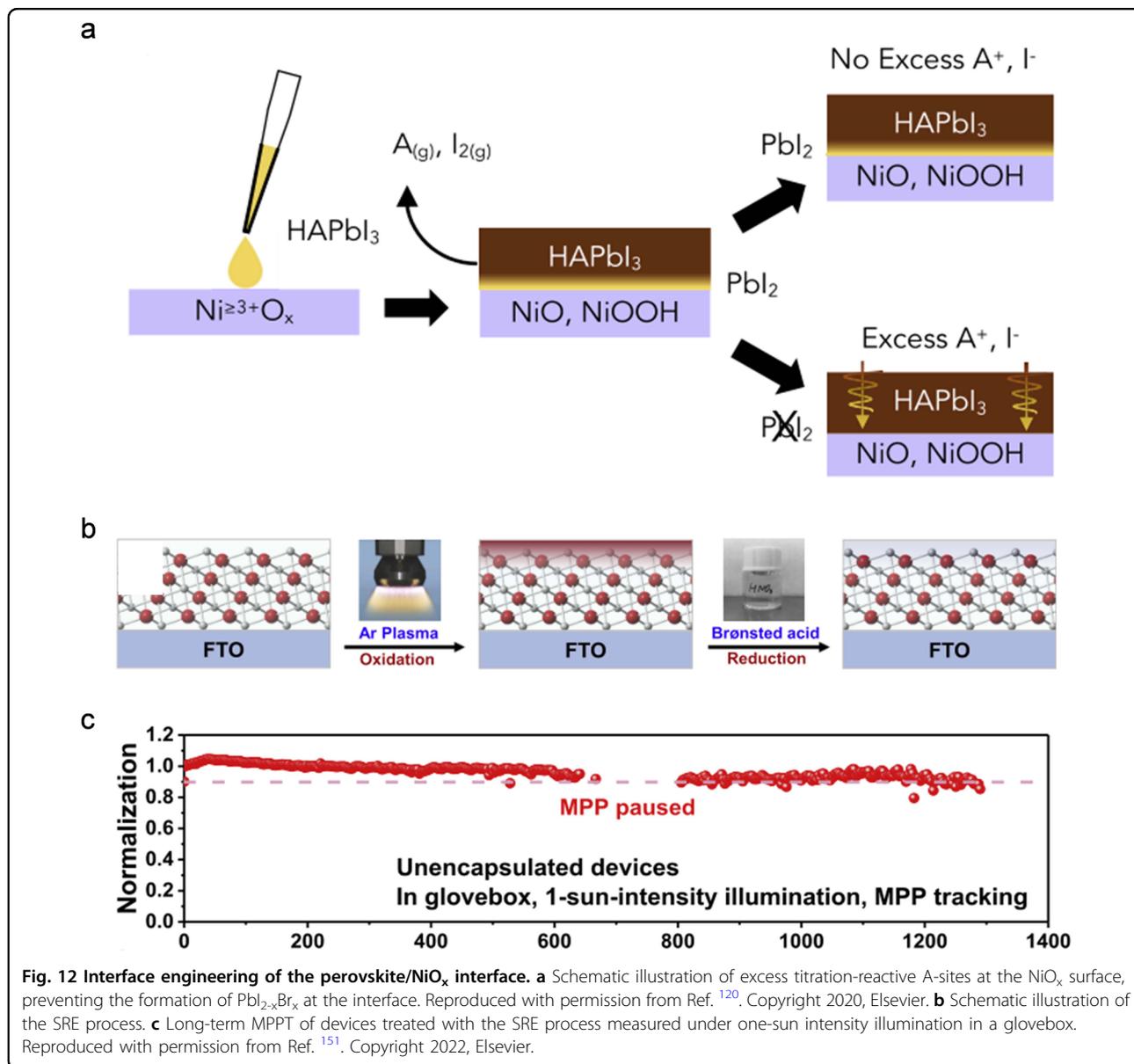
To further narrow the efficiency gap, Zhu et al. proposed an organometallic compound, ferrocenyl-bis-thiophene-2-carboxylate (FcTc₂), as a functionalization material for the perovskite/ C_{60} interface (Fig. 11d)¹⁸, which not only reduced the surface traps *via* strong chemical Pb-O binding but also improved interfacial electron transfer through the electron-rich and electron-delocalizing ferrocene units. Leveraging these benefits, inverted PSCs with FcTc₂ passivation achieved an astonishing certified PCE of 24.3% ($V_{OC} = 1.179$ V, $J_{SC} = 25.59$ mA cm⁻², and FF = 80.60%), which was the first time a certified PCE of more than 24% was achieved by inverted PSCs. The resulting PSCs also exhibited superior stability, successfully passing international standards (IEC61215:2016) under the damp-heat test (85 °C and 85% RH). Recently, Zhu et al. introduced a reactive surface engineering approach based on the simple post-treatment of 3-(aminomethyl)pyridine (3-APy) on top of perovskite films to push the efficiency of inverted PSCs to its limit. As shown in Fig. 11e¹⁹, the 3-APy molecule could selectively react with surface FA⁺, reducing the perovskite surface roughness. In addition, the perovskite surface region became more n-type due to the reduction in the formation energy of charged iodine vacancies induced by the reaction product on the perovskite surface, which was favorable for facilitating electron transport. Based on these advantages, the inverted PSC achieved the highest certified PCE of 25.37% according to the J - V characteristics measured by NREL. Moreover, the resulting PSCs also exhibited excellent operational stability, retaining 87% of their initial PCE after over 2400 h under one-sun illumination at approximately 55 °C in air.

In addition to improving the properties of the perovskite/ETM interface, defect passivation between the hole-selective contact layer and perovskite interface is also



an effective way to fabricate efficient and stable inverted PSCs, especially the defect passivation strategy for the NiO_x/perovskite interface^{112,120}. As mentioned above, the complex surface chemical properties of NiO_x cause many difficult issues at the NiO_x/perovskite interface, limiting the further improvement of NiO_x-based inverted PSCs. In particular, Ni^{≥3+} cation sites on the surface of NiO_x as Brønsted proton acceptors and Lewis electron acceptors induce the formation of PbI_{2-x}Br_x at the NiO_x/perovskite

interface, which increases recombination at the interface and acts as a hole extraction barrier, due to their capability of deprotonating cationic amines and oxidizing iodide species in perovskite films^{120,121}, thus impairing the device performance. To this end, McGehee et al. provided a simple approach to alter the perovskite precursor stoichiometry with excess FAI to react with the Ni^{≥3+} cation sites (Fig. 12a)¹²⁰. The resulting PSCs based on a NiO_x-HTM with a Cs_{0.25}FA_{0.75}Pb(Br_{0.2}I_{0.8})₃ perovskite layer



achieved a high PCE of 19.66% with a high V_{OC} of 1.14 V. In addition, vacuum-treated NiO_x films have poor surface wettability, which weakens the adhesion of perovskite ink and creates challenges for the deposition of large-area perovskite films. The high-oxidative-state $\text{Ni}^{\geq 3+}$ species on the surface also react with the perovskite, resulting in the formation of hole extraction barriers and severe chemical degradation at the NiO_x /perovskite interface. In this regard, Liu et al. proposed surface redox engineering (SRE) for vacuum-deposited NiO_x to make it suitable for slot-die-coated perovskite films. In brief, the SRE method involved continuously subjecting the NiO_x films to an Ar-plasma-initiated oxidation process and a Brønsted acid (HNO_3)-mediated reduction process (Fig. 12b)¹⁵¹, which

not only improved the wetting property of the perovskite ink on the surface of vacuum-deposited NiO_x but also prevented adverse chemical reactions and improved the energy-band alignment at the NiO_x /perovskite interface. As a result, the inverted PSCs with NiO_x as the HTM achieved excellent PCEs of 23.4% and 21.3% in rigid and flexible devices, respectively. The unencapsulated SRE-PSCs also showed superior operational stability, retaining 90% of their initial efficiency under MPPT and continuous one-sun illumination in a glovebox for over 1300 h (Fig. 12c). Furthermore, the perovskite submodules with a high-quality perovskite film fabricated *via* slot-die coating successfully exhibited a remarkable PCE of 18.6% with an area of $156 \times 156 \text{ mm}^2$. Recently, Qi et al. also found that

the oxidation of iodide and the generation of free protons at the NiO_x /perovskite interface under one-sun illumination resulted in multistep undesired photochemical reactions, leading to the photodegradation of inverted PSCs based on NiO_x ¹²¹. They proposed a trimethylsulfonium bromide (TMSBr) buffer layer at the NiO_x /perovskite interface to overcome this photodegradation. The unique properties of aprotic TMS⁺ allow it to prevent contact reaction between perovskite and NiO_x and maintain the lattice coherence as well as suppress the trap density. The resulting inverted PSCs with the TMSBr buffer layer showed superior long-term operational stability and retained 82.8% of their initial PCE after continuous operation for 2000 h under AM1.5 G light illumination.

Based on the above discussion, interface engineering plays an important role in fabricating high-efficiency inverted PSCs. An important reason for implementing interface engineering is that there is too much non-radiative recombination at the interface, which is attributed to carrier recombination induced by defect states and dangling bonds¹⁵². For the interface engineering of inverted PSCs, the following should be noted: (i) First, to reduce carrier recombination at the interface, the carrier separation speed should be fast, which is mainly determined by the built-in electric field (V_{bi} , closely related to the V_{OC} of the device) generated by the p-n junction at the interface. Interface engineering should be an effective way to enhance V_{bi} with the driving force of charge separation (electrons and holes moving toward two opposite interfaces). (ii) Second, carrier extraction should be rapid and determined by the energy level alignment at the perovskite/CTM interface, which is the key to effective charge extraction. Briefly, the energy level of conduction band (E_c) of the perovskite layer should be higher than that of the ETM, while the energy level of valence band (E_v) should be lower than that of the HTM. Interface engineering has been employed to efficiently tune the energy level alignment and reduce the carrier band offset, thereby suppressing interfacial recombination. (iii) High carrier mobilities of CTMs are equally important for interfacial charge dynamics. Therefore, the interlayers should have functional groups and high conductivity, which can allow the passivation of interfacial defects and minimize carrier losses with interface dipoles, thereby achieving favorable charge dynamics at interfaces. (iv) In addition to the functions mentioned above, the interlayer should also improve the stability of devices. For example, an FcTc_2 interlayer promoted carrier transfer through its organic functional groups and formed strong chemical Pb-O binding to reduce the defect states on the perovskite surface¹⁸, thus improving device stability. (v) At present, interface engineering, mainly involving spin coating methods, is extensively used for small-area PSCs (typically

active area $<1 \text{ cm}^2$), but it is a challenge to use for large-area modules. Methods such as thermal evaporation, screen printing, and atomic layer deposition should be developed to deposit a dense and uniform interface layer for high-efficiency and large-area inverted PSCs.

Conclusions and future perspectives

Inverted PSCs have been developed rapidly in recent years. Great efforts have been made to increase the efficiencies of inverted PSCs with small aperture areas from 3.9%²³ to 25.37%¹⁹ by improving the quality of perovskite films and developing appropriate CTMs and various defect passivation strategies. A perovskite mini-module with an inverted structure also achieved a high certified PCE of 21.07%²⁷. Regarding stability, both small-area inverted PSCs^{18,20} and perovskite mini-modules¹⁵³ with an inverted structure have passed international standard (IEC 61215:2016) tests (under damp heat at 85 °C and 85% RH), indicating the commercialization prospects of inverted PSCs. Nevertheless, there is still a certain gap between the certified stabilized efficiency of inverted PSCs and regular PSCs (24.05% *versus* 25.7%). Therefore, more efforts are needed to improve the efficiency of inverted PSCs to compete with other counterpart solar cells, for which the following steps are proposed.

(1) HTMs greatly influence the J_{SC} of inverted PSCs. For example, the J_{SC} of NiO_x -based inverted PSCs is generally lower than that of PTAA-based PSCs^{17,18}. Therefore, more suitable CTMs should be developed because the CTM determines the carrier separation and transfer in a PSC.

(2) Most inverted PSCs with efficiencies greater than 23% are based on organic HTMs, such as PTAA and SAMs. However, organic HTMs can be degraded in moist and high-temperature environments. Recently, inverted PSCs based on common organic HTMs (PTAA or 2PACz) passed the international standard test (IEC61215:2016) under damp heat (85 °C and 85% RH), showing great commercialization prospects. In contrast, organic HTMs are generally expensive, which limits the application of PSCs. In addition, inverted PSCs with PTAA exhibit inferior stability compared with NiO_x -based devices, which suffer from more serious interface deterioration and bulk decomposition by forming voids by releasing I_2 gas from defective regions at grain boundaries under continuous exposure to light and heat¹⁵⁴. As the most promising inorganic HTM at present, NiO_x has the advantages of low synthesis cost, good environmental stability, and excellent thermal stability, which have led to its application in inverted PSCs¹¹². However, due to poor intrinsic conductivity and various surface trap states, the efficiencies of NiO_x -based inverted devices remain low as an obstacle to their commercialization. Therefore, more efforts are needed to improve the film quality of NiO_x itself, including surface modification or doping of NiO_x , to achieve

high photoelectric properties comparable to those of common organic HTMs and to achieve a competitive efficiency of 25%.

(3) Encapsulation technology is very important for device stability. Encapsulated devices are usually used for thermal stability and operational stability tests, indicating that encapsulation technology is crucial to improving device stability. Here, integrating effective barriers into PSCs as internal encapsulation technologies plays an important role in device stability. This can shield the perovskite layer from external moisture erosion and prevent undesirable ion diffusion. For instance, Han et al. introduced low-dimensional diffusion barriers (DBLs) on top of perovskite films to reduce the detrimental interfacial diffusion of ions¹⁵³. Consequently, the perovskite solar modules successfully passed the industry-relevant damp-heat test (85 °C and 85% RH). In addition, external encapsulation technology is also commonly used in the field of PSCs due to its low cost and effective blocking of moisture and oxygen penetration¹⁵⁵. For example, Lidzey et al. introduced a solution-processable polymer interlayer (polyvinylpyrrolidone (PVP)) between a PSC and epoxy covered with a glass encapsulation slide¹⁵⁶, which significantly improved the stability of the corresponding inverted PSCs with a T_{80} lifetime of 1000 h. Although it was reported that the encapsulated inverted devices passed the industry-relevant damp-heat test (85 °C and 85% RH)^{18,20}, few reports have shown that PSCs pass stability tests certified by a third party, underscoring the significance of developing encapsulation technology for inverted PSCs, which is the key to promoting the commercialization of inverted PSCs.

The urgent issue for inverted PSCs is to improve their steady-state PCE ($\geq 25\%$) and long-term stability, which can significantly reduce the cost of inverted devices, thus accelerating their commercialization.

Acknowledgements

This work was financially supported by the National Key Research and Development Project funding from the National Natural Science Foundation of China (Grant Nos. 52002140, U20A20252), the Ministry of Science and Technology of China (Grant No. 2021YFB3800104), Young Elite Scientists Sponsorship Program by CAST, the Self-determined and Innovative Research Funds of HUST (2020kfyXJJS008), the Natural Science Foundation of Hubei Province (2022CFA093), and the Innovation Project of Optics Valley Laboratory (Grant No. OVL2021BG008). V.B. acknowledges a MEXT JSPS Grant-in-Aid for Scientific Research (19H02550), a JSPS-DST bilateral research grant, and the Dynamic Alliance for Open Innovation Bridging Human, Environment, and Materials. Y.B.Q. acknowledges the support from the Energy Materials and Surface Sciences Unit of the Okinawa Institute of Science and Technology Graduate University.

Author details

¹Wuhan National Laboratory for Optoelectronics (WNLO), Huazhong University of Science and Technology (HUST), Wuhan, China. ²Research Institute for Electronic Science, Hokkaido University, Sapporo, Hokkaido, Japan. ³Graduate School of Environmental Science, Hokkaido University, Sapporo, Hokkaido, Japan. ⁴Energy Materials and Surface Sciences Unit (EMSSU), Okinawa Institute

of Science and Technology Graduate University (OIST), Okinawa, Japan. ⁵Optics Valley Laboratory, Hubei, China

Author contributions

All the authors contributed to the writing, review, and editing of the manuscript.

Conflict of interest

The authors declare no competing interests.

Publisher's note

Springer Nature remains neutral with regard to jurisdictional claims in published maps and institutional affiliations.

Received: 29 November 2022 Revised: 1 March 2023 Accepted: 7 March 2023.

Published online: 5 May 2023

References

- Best Research-Cell Efficiency Chart. <https://www.nrel.gov/pv/cell-efficiency.html>.
- Min, H. et al. Perovskite solar cells with atomically coherent interlayers on SnO₂ electrodes. *Nature* **598**, 444–450 (2021).
- Zhao, Y. et al. Inactive (PbI₂)₂RbCl stabilizes perovskite films for efficient solar cells. *Science* **377**, 531–534 (2022).
- Yoo, J. J. et al. Efficient perovskite solar cells via improved carrier management. *Nature* **590**, 587–593 (2021).
- Lee, M. M., Teuscher, J., Miyasaka, T., Murakami, T. N. & Snaith, H. J. Efficient hybrid solar cells based on meso-superstructured organometal halide perovskites. *Science* **338**, 643–647 (2012).
- Kim, M. et al. Enhanced electrical properties of Li-salts doped mesoporous TiO₂ in perovskite solar cells. *Joule* **5**, 659–672 (2021).
- Jiang, Q. et al. Enhanced electron extraction using SnO₂ for high-efficiency planar-structure HC(NH₂)₂PbI₃-based perovskite solar cells. *Nat. Energy* **2**, 1–7 (2016).
- Jiang, Q. et al. Planar-structure perovskite solar cells with efficiency beyond 21%. *Adv. Mater.* **29**, 1703852 (2017).
- Jiang, Q. et al. Surface passivation of perovskite film for efficient solar cells. *Nat. Photonics* **13**, 460–466 (2019).
- Chen, Y. et al. Self-elimination of intrinsic defects improves the low-temperature performance of perovskite photovoltaics. *Joule* **4**, 1961–1976 (2020).
- Bu, T. et al. Universal passivation strategy to slot-die printed SnO₂ for hysteresis-free efficient flexible perovskite solar module. *Nat. Commun.* **9**, 1–10 (2018).
- Jeong, M. et al. Large-area perovskite solar cells employing spiro-Naph hole transport material. *Nat. Photonics* **16**, 119–125 (2022).
- Ren, G. et al. Strategies of modifying spiro-OMeTAD materials for perovskite solar cells: a review. *J. Mater. Chem. A* **9**, 4589–4625 (2021).
- Rombach, F. M., Haque, S. A. & Macdonald, T. J. Lessons learned from spiro-OMeTAD and PTAA in perovskite solar cells. *Energy Environ. Sci.* **14**, 5161–5190 (2021).
- Lin, Y.-H. et al. A piperidinium salt stabilizes efficient metal-halide perovskite solar cells. *Science* **369**, 96–102 (2020).
- Li, X. et al. Constructing heterojunctions by surface sulfidation for efficient inverted perovskite solar cells. *Science* **375**, 434–437 (2022).
- Chen, H. et al. Quantum-size-tuned heterostructures enable efficient and stable inverted perovskite solar cells. *Nat. Photonics* **16**, 352–358 (2022).
- Li, Z. et al. Organometallic-functionalized interfaces for highly efficient inverted perovskite solar cells. *Science* **376**, 416–420 (2022).
- Jiang, Q. et al. Surface reaction for efficient and stable inverted perovskite solar cells. *Nature* **611**, 278–283 (2022).
- Azmi, R. et al. Damp heat-stable perovskite solar cells with tailored-dimensionality 2D/3D heterojunctions. *Science* **376**, 73–77 (2022).
- Al-Ashouri, A. et al. Monolithic perovskite/silicon tandem solar cell with >29% efficiency by enhanced hole extraction. *Science* **370**, 1300–1309 (2020).

22. Lin, R. et al. All-perovskite tandem solar cells with improved grain surface passivation. *Nature* **603**, 73–78 (2022).
23. Jeng, J. Y. et al. $\text{CH}_3\text{NH}_3\text{PbI}_3$ perovskite/fullerene planar-heterojunction hybrid solar cells. *Adv. Mater.* **25**, 3727–3732 (2013).
24. Chen, W. et al. Efficient and stable large-area perovskite solar cells with inorganic charge extraction layers. *Science* **350**, 944–948 (2015).
25. Zheng, X. et al. Managing grains and interfaces via ligand anchoring enables 22.3%-efficiency inverted perovskite solar cells. *Nat. Energy* **5**, 131–140 (2020).
26. Chen, S. et al. Stabilizing perovskite-substrate interfaces for high-performance perovskite modules. *Science* **373**, 902–907 (2021).
27. Gao, Y. et al. Can nanosecond laser achieve high-performance perovskite solar modules with aperture area efficiency over 21%? *Adv. Energy Mater.* **12**, 2202287 (2022).
28. Green, M. A. et al. Solar cell efficiency tables (Version 60). *Prog. Photovolt. Res. Appl.* **30**, 687–701 (2022).
29. Stolterfoht, M. et al. The impact of energy alignment and interfacial recombination on the internal and external open-circuit voltage of perovskite solar cells. *Energy Environ. Sci.* **12**, 2778–2788 (2019).
30. Caprioglio, P. et al. On the relation between the open-circuit voltage and quasi-fermi level splitting in efficient perovskite solar cells. *Adv. Energy Mater.* **9**, 1901631 (2019).
31. Shockley, W. & Queisser, H. J. Detailed balance limit of efficiency of p-n junction solar cells. *J. Appl. Phys.* **32**, 510–519 (1961).
32. Saliba, M. et al. Cesium-containing triple cation perovskite solar cells: improved stability, reproducibility and high efficiency. *Energy Environ. Sci.* **9**, 1989–1997 (2016).
33. Lee, J. W. et al. Formamidinium and cesium hybridization for photo- and moisture-stable perovskite solar cell. *Adv. Energy Mater.* **5**, 1501310 (2015).
34. Pellet, N. et al. Mixed-organic-cation perovskite photovoltaics for enhanced solar-light harvesting. *Angew. Chem. Int. Ed.* **126**, 3215–3221 (2014).
35. McMeekin, D. P. et al. A mixed-cation lead mixed-halide perovskite absorber for tandem solar cells. *Science* **351**, 151–155 (2016).
36. Chen, W. et al. Hybrid interfacial layer leads to solid performance improvement of inverted perovskite solar cells. *Energy Environ. Sci.* **8**, 629–640 (2015).
37. Lee, K.-M. et al. Selection of anti-solvent and optimization of dropping volume for the preparation of large area sub-module perovskite solar cells. *Sol. Energy Mater. Sol. Cells* **172**, 368–375 (2017).
38. Chen, C. et al. Understanding the effect of antisolvent on processing window and efficiency for large-area flexible perovskite solar cells. *Mater. Today Phys.* **21**, 100565 (2021).
39. Li, M. et al. Comparison of processing windows and electronic properties between $\text{CH}_3\text{NH}_3\text{PbI}_3$ perovskite fabricated by one-step and two-step solution processes. *Org. Electron.* **63**, 159–165 (2018).
40. Roß, M. et al. Co-evaporated formamidinium lead iodide based perovskites with 1000 h constant stability for fully textured monolithic perovskite/silicon tandem solar cells. *Adv. Energy Mater.* **11**, 2101460 (2021).
41. Wu, W.-Q. et al. Bilateral alkylamine for suppressing charge recombination and improving stability in blade-coated perovskite solar cells. *Sci. Adv.* **5**, eaav8925 (2019).
42. Subbiah, A. S. et al. High-performance perovskite single-junction and textured perovskite/silicon tandem solar cells via slot-die-coating. *ACS Energy Lett.* **5**, 3034–3040 (2020).
43. Turren-Cruz, S.-H., Hagfeldt, A. & Saliba, M. Methylammonium-free, high-performance, and stable perovskite solar cells on a planar architecture. *Science* **362**, 449–453 (2018).
44. Conings, B. et al. Intrinsic thermal instability of methylammonium lead trihalide perovskite. *Adv. Energy Mater.* **5**, 1500477 (2015).
45. Juarez-Perez, E. J., Ono, L. K. & Qi, Y. B. Thermal degradation of formamidinium based lead halide perovskites into sym-triazine and hydrogen cyanide observed by coupled thermogravimetry-mass spectrometry analysis. *J. Mater. Chem. A* **7**, 16912–16919 (2019).
46. Yang, W. S. et al. High-performance photovoltaic perovskite layers fabricated through intramolecular exchange. *Science* **348**, 1234–1237 (2015).
47. Zhao, Y. & Zhu, K. Organic–inorganic hybrid lead halide perovskites for optoelectronic and electronic applications. *Chem. Soc. Rev.* **45**, 655–689 (2016).
48. Zheng, X. et al. Defect passivation in hybrid perovskite solar cells using quaternary ammonium halide anions and cations. *Nat. Energy* **2**, 1–9 (2017).
49. Yi, C. et al. Entropic stabilization of mixed A-cation ABX_3 metal halide perovskites for high performance perovskite solar cells. *Energy Environ. Sci.* **9**, 656–662 (2016).
50. Fiscaro, G. et al. Local order and rotational dynamics in mixed A-cation lead iodide perovskites. *J. Phys. Chem. Lett.* **11**, 1068–1074 (2020).
51. Ghosh, D., Smith, A. R., Walker, A. B. & Islam, M. S. Mixed A-cation perovskites for solar cells: atomic-scale insights into structural distortion, hydrogen bonding, and electronic properties. *Chem. Mater.* **30**, 5194–5204 (2018).
52. Chen, B. et al. Passivation of the buried interface via preferential crystallization of 2D perovskite on metal oxide transport layers. *Adv. Mater.* **33**, 2103394 (2021).
53. Masi, S. et al. Chemi-structural stabilization of formamidinium lead iodide perovskite by using embedded quantum dots. *ACS Energy Lett.* **5**, 418–427 (2020).
54. Nan, Z.-A. et al. Revealing phase evolution mechanism for stabilizing formamidinium-based lead halide perovskites by a key intermediate phase. *Chem* **7**, 2513–2526 (2021).
55. Kim, M. et al. Methylammonium chloride induces intermediate phase stabilization for efficient perovskite solar cells. *Joule* **3**, 2179–2192 (2019).
56. Min, H. et al. Efficient, stable solar cells by using inherent bandgap of α -phase formamidinium lead iodide. *Science* **366**, 749–753 (2019).
57. Zhang, Y. et al. Propylammonium chloride additive for efficient and stable FAPbI₃ perovskite solar cells. *Adv. Energy Mater.* **11**, 2102538 (2021).
58. Zhang, D. et al. Stable α -FAPbI₃ in inverted perovskite solar cells with efficiency exceeding 22% via a self-passivation strategy. *Adv. Funct. Mater.* **32**, 2200174 (2022).
59. Xie, F. X. et al. Vacuum-assisted thermal annealing of $\text{CH}_3\text{NH}_3\text{PbI}_3$ for highly stable and efficient perovskite solar cells. *ACS Nano* **9**, 639–646 (2015).
60. Malinkiewicz, O. et al. Perovskite solar cells employing organic charge-transport layers. *Nat. Photonics* **8**, 128–132 (2014).
61. Mombiona, C. et al. Efficient vacuum deposited pin and nip perovskite solar cells employing doped charge transport layers. *Energy Environ. Sci.* **9**, 3456–3463 (2016).
62. Chiang, Y.-H., Anaya, M. & Stranks, S. D. Multisource vacuum deposition of methylammonium-free perovskite solar cells. *ACS Energy Lett.* **5**, 2498–2504 (2020).
63. Choi, Y. et al. A vertically oriented two-dimensional Ruddlesden–Popper phase perovskite passivation layer for efficient and stable inverted perovskite solar cells. *Energy Environ. Sci.* **15**, 3369–3378 (2022).
64. Jeong, J. et al. The introduction of a perovskite seed layer for high performance perovskite solar cells. *J. Mater. Chem. A* **6**, 20138–20144 (2018).
65. Xiao, Z. et al. Solvent annealing of perovskite-induced crystal growth for photovoltaic-device efficiency enhancement. *Adv. Mater.* **26**, 6503–6509 (2014).
66. Wu, C.-G. et al. High efficiency stable inverted perovskite solar cells without current hysteresis. *Energy Environ. Sci.* **8**, 2725–2733 (2015).
67. Chiang, C.-H., Nazeeruddin, M. K., Gratzel, M. & Wu, C.-G. The synergistic effect of H_2O and DMF towards stable and 20% efficiency inverted perovskite solar cells. *Energy Environ. Sci.* **10**, 808–817 (2017).
68. Gutierrez-Partida, E. et al. Large-grain double cation perovskites with 18 μs lifetime and high luminescence yield for efficient inverted perovskite solar cells. *ACS Energy Lett.* **6**, 1045–1054 (2021).
69. Shao, Y., Yuan, Y. & Huang, J. Correlation of energy disorder and open-circuit voltage in hybrid perovskite solar cells. *Nat. Energy* **1**, 1–6 (2016).
70. Seo, J. et al. Benefits of very thin PCBM and LiF layers for solution-processed p–i–n perovskite solar cells. *Energy Environ. Sci.* **7**, 2642–2646 (2014).
71. Jeon, N. J. et al. Solvent engineering for high-performance inorganic-organic hybrid perovskite solar cells. *Nat. Mater.* **13**, 897–903 (2014).
72. Xiao, M. et al. A fast deposition-crystallization procedure for highly efficient lead iodide perovskite thin-film solar cells. *Angew. Chem. Int. Ed.* **53**, 9898–9903 (2014).
73. Taylor, A. D. et al. A general approach to high-efficiency perovskite solar cells by any antisolvent. *Nat. Commun.* **12**, 1–11 (2021).
74. Huang, F. et al. Gas-assisted preparation of lead iodide perovskite films consisting of a monolayer of single crystalline grains for high efficiency planar solar cells. *Nano Energy* **10**, 10–18 (2014).
75. Li, X. et al. A vacuum flash–assisted solution process for high-efficiency large-area perovskite solar cells. *Science* **353**, 58–62 (2016).
76. Bu, T. et al. Dynamic antisolvent engineering for spin coating of $10 \times 10 \text{ cm}^2$ perovskite solar module approaching 18%. *Sol. RRL* **4**, 1900263 (2020).

77. Park, N.-G. & Zhu, K. Scalable fabrication and coating methods for perovskite solar cells and solar modules. *Nat. Rev. Mater.* **5**, 333–350 (2020).
78. Deng, Y. et al. Tailoring solvent coordination for high-speed, room-temperature blading of perovskite photovoltaic films. *Sci. Adv.* **5**, eaax7537 (2019).
79. Yang, Z. et al. Slot-die coating large-area formamidinium-cesium perovskite film for efficient and stable parallel solar module. *Sci. Adv.* **7**, eabg3749 (2021).
80. Zimmermann, I. et al. Sequentially slot-die-coated perovskite for efficient and scalable solar cells. *Adv. Mater. Interfaces* **8**, 2100743 (2021).
81. Lee, D.-K., Jeong, D.-N., Ahn, T. K. & Park, N.-G. Precursor engineering for a large-area perovskite solar cell with > 19% efficiency. *ACS Energy Lett.* **4**, 2393–2401 (2019).
82. Lee, J.-W. et al. Tuning molecular interactions for highly reproducible and efficient formamidinium perovskite solar cells via adduct approach. *J. Am. Chem. Soc.* **140**, 6317–6324 (2018).
83. Li, Y. et al. Poly (3, 4-Ethylenedioxythiophene): methylnaphthalene sulfonate formaldehyde condensate: the effect of work function and structural homogeneity on hole injection/extraction properties. *Adv. Energy Mater.* **7**, 1601499 (2017).
84. Zhao, D. et al. High-efficiency solution-processed planar perovskite solar cells with a polymer hole transport layer. *Adv. Energy Mater.* **5**, 1401855 (2015).
85. Yao, Y. et al. Organic hole transport layers for efficient, stable and scalable inverted perovskite solar cells. *Adv. Mater.* **34**, 2203794 (2022).
86. Liu, Z. et al. Interfacial engineering of front-contact with finely tuned polymer interlayers for high-performance large-area flexible perovskite solar cells. *Nano Energy* **62**, 734–744 (2019).
87. Wang, C. et al. MoO₃ doped PTAA for high-performance inverted perovskite solar cells. *Appl. Surf. Sci.* **571**, 151301 (2022).
88. Dong, W. et al. Black phosphorus doped poly (triarylamine) as hole transport layer for highly efficient perovskite solar cells. *Org. Electron.* **89**, 106052 (2021).
89. Wang, Q., Bi, C. & Huang, J. Doped hole transport layer for efficiency enhancement in planar heterojunction organolead trihalide perovskite solar cells. *Nano Energy* **15**, 275–280 (2015).
90. Zhao, Q. et al. Achieving efficient inverted planar perovskite solar cells with nondoped PTAA as a hole transport layer. *Org. Electron.* **71**, 106–112 (2019).
91. Bi, C. et al. Non-wetting surface-driven high-aspect-ratio crystalline grain growth for efficient hybrid perovskite solar cells. *Nat. Commun.* **6**, 7747 (2015).
92. Isikgor, F. H. et al. Scaling-up perovskite solar cells on hydrophobic surfaces. *Nano Energy* **81**, 105633 (2021).
93. You, J. et al. The fabrication of homogeneous perovskite films on non-wetting interfaces enabled by physical modification. *J. Energy Chem.* **38**, 192–198 (2019).
94. Liu, X. et al. 20.7% highly reproducible inverted planar perovskite solar cells with enhanced fill factor and eliminated hysteresis. *Energy Environ. Sci.* **12**, 1622–1633 (2019).
95. Chen, R. et al. Robust hole transport material with interface anchors enhances the efficiency and stability of inverted formamidinium-cesium perovskite solar cells with a certified efficiency of 22.3%. *Energy Environ. Sci.* **15**, 2567–2580 (2022).
96. Sun, X. et al. Efficient inverted perovskite solar cells with low voltage loss achieved by a pyridine-based dopant-free polymer semiconductor. *Angew. Chem. Int. Ed.* **60**, 7227–7233 (2021).
97. Xu, X. et al. Improving contact and passivation of buried interface for high-efficiency and large-area inverted perovskite solar cells. *Adv. Funct. Mater.* **32**, 2109968 (2022).
98. Wang, Y. et al. Teaching an old anchoring group new tricks: enabling low-cost, eco-friendly hole-transporting materials for efficient and stable perovskite solar cells. *J. Am. Chem. Soc.* **142**, 16632–16643 (2020).
99. Zhang, L. et al. Hole-transporting layer based on a conjugated polyelectrolyte with organic cations enables efficient inverted perovskite solar cells. *Nano Energy* **57**, 248–255 (2019).
100. Ullah, A. et al. Versatile hole selective molecules containing a series of heteroatoms as self-assembled monolayers for efficient p-i-n perovskite and organic solar cells. *Adv. Funct. Mater.* **32**, 2208793 (2022).
101. Kim, G.-H. et al. High-efficiency colloidal quantum dot photovoltaics via robust self-assembled monolayers. *Nano Lett.* **15**, 7691–7696 (2015).
102. Magomedov, A. et al. Self-assembled hole transporting monolayer for highly efficient perovskite solar cells. *Adv. Energy Mater.* **8**, 1801892 (2018).
103. Al-Ashouri, A. et al. Conformal monolayer contacts with lossless interfaces for perovskite single junction and monolithic tandem solar cells. *Energy Environ. Sci.* **12**, 3356–3369 (2019).
104. Deng, X. et al. Co-assembled monolayers as hole-selective contact for high-performance inverted perovskite solar cells with optimized recombination loss and long-term stability. *Angew. Chem. Int. Ed.* **61**, e202203088 (2022).
105. Liao, Q. et al. Self-assembled donor-acceptor hole contacts for inverted perovskite solar cells with an efficiency approaching 22%: The impact of anchoring groups. *J. Energy Chem.* **68**, 87–95 (2022).
106. Chen, W. et al. Engineering of dendritic dopant-free hole transport molecules: enabling ultrahigh fill factor in perovskite solar cells with optimized dendron construction. *Sci. China Chem.* **64**, 41–51 (2021).
107. Wang, Y. et al. Dopant-free small-molecule hole-transporting material for inverted perovskite solar cells with efficiency exceeding 21%. *Adv. Mater.* **31**, 1902781 (2019).
108. Chen, S., Xiao, X., Gu, H. & Huang, J. Iodine reduction for reproducible and high-performance perovskite solar cells and modules. *Sci. Adv.* **7**, eabe8130 (2021).
109. Chen, Y. et al. Thermally stable methylammonium-free inverted perovskite solar cells with Zn²⁺ doped CuGaO₂ as efficient mesoporous hole-transporting layer. *Nano Energy* **61**, 148–157 (2019).
110. Zhang, H. et al. Low-temperature solution-processed CuCrO₂ hole-transporting layer for efficient and photostable perovskite solar cells. *Adv. Energy Mater.* **8**, 1702762 (2018).
111. Kakavelakis, G. et al. Extending the continuous operating lifetime of perovskite solar cells with a molybdenum disulfide hole extraction interlayer. *Adv. Energy Mater.* **8**, 1702287 (2018).
112. Ma, F. et al. Nickel oxide for inverted structure perovskite solar cells. *J. Energy Chem.* **52**, 393–411 (2021).
113. Wei, Y. et al. Improving the efficiency and environmental stability of inverted planar perovskite solar cells via silver-doped nickel oxide hole-transporting layer. *Appl. Surf. Sci.* **427**, 782–790 (2018).
114. Xiao, S. et al. An ultra-low concentration of gold nanoparticles embedded in the NiO hole transport layer boosts the performance of p-i-n perovskite solar cells. *Sol. RRL* **3**, 1800278 (2019).
115. Chen, W. et al. Understanding the doping effect on NiO: toward high-performance inverted perovskite solar cells. *Adv. Energy Mater.* **8**, 1703519 (2018).
116. Chen, W. et al. Cesium doped NiO_x as an efficient hole extraction layer for inverted planar perovskite solar cells. *Adv. Energy Mater.* **7**, 1700722 (2017).
117. Chen, W. et al. Alkali chlorides for the suppression of the interfacial recombination in inverted planar perovskite solar cells. *Adv. Energy Mater.* **9**, 1803872 (2019).
118. Chen, W. et al. Molecule-doped nickel oxide: verified charge transfer and planar inverted mixed cation perovskite solar cell. *Adv. Mater.* **30**, 1800515 (2018).
119. Ru, P. et al. High electron affinity enables fast hole extraction for efficient flexible inverted perovskite solar cells. *Adv. Energy Mater.* **10**, 1903487 (2020).
120. Boyd, C. C. et al. Overcoming redox reactions at perovskite-nickel oxide interfaces to boost voltages in perovskite solar cells. *Joule* **4**, 1759–1775 (2020).
121. Wu, T. et al. Elimination of light-induced degradation at the nickel oxide-perovskite heterojunction by aprotic sulfonium layers towards long-term operationally stable inverted perovskite solar cells. *Energy Environ. Sci.* **15**, 4612–4624 (2022).
122. Zhu, X. et al. Inverted planar heterojunction perovskite solar cells with high ultraviolet stability. *Nano Energy* **103**, 107849 (2022).
123. Yang, B., Peng, S. & Choy, W. C. Inorganic top electron transport layer for high performance inverted perovskite solar cells. *EcoMat* **3**, e12127 (2021).
124. Kim, M. et al. Conformal quantum dot-SnO₂ layers as electron transporters for efficient perovskite solar cells. *Science* **375**, 302–306 (2022).
125. Fang, R. et al. [6, 6]-Phenyl-C₆₁-butyric acid methyl ester/cesium oxide bilayer structure as efficient and stable electron transport layer for inverted perovskite solar cells. *ACS Nano* **12**, 2403–2414 (2018).
126. Troughton, J. et al. A universal solution processed interfacial bilayer enabling ohmic contact in organic and hybrid optoelectronic devices. *Energy Environ. Sci.* **13**, 268–276 (2020).
127. Xiao, K. et al. Scalable processing for realizing 21.7%-efficient all-perovskite tandem solar modules. *Science* **376**, 762–767 (2022).

128. Wu, S. et al. A chemically inert bismuth interlayer enhances long-term stability of inverted perovskite solar cells. *Nat. Commun.* **10**, 1–11 (2019).
129. Li, X. et al. Chemical anti-corrosion strategy for stable inverted perovskite solar cells. *Sci. Adv.* **6**, eabd1580 (2020).
130. Chen, C. et al. Effect of BCP buffer layer on eliminating charge accumulation for high performance of inverted perovskite solar cells. *RSC Adv.* **7**, 35819–35826 (2017).
131. Guo, S. et al. Non-uniform chemical corrosion of metal electrode of p–i–n type of perovskite solar cells caused by the diffusion of $\text{CH}_3\text{NH}_3\text{I}$. *Energy Technol.* **8**, 2000250 (2020).
132. Ning, J. et al. Gaining insight into the effect of organic interface layer on suppressing ion migration induced interfacial degradation in perovskite solar cells. *Adv. Funct. Mater.* **30**, 2000837 (2020).
133. Parida, B. et al. Boosting the conversion efficiency over 20% in MAPbI_3 perovskite planar solar cells by employing a solution-processed aluminum-doped nickel oxide hole collector. *ACS Appl. Mater. Interfaces* **12**, 22958–22970 (2020).
134. Chen, W., Xu, L., Feng, X., Jie, J. & He, Z. Metal acetylacetonate series in interface engineering for full low-temperature-processed, high-performance, and stable planar perovskite solar cells with conversion efficiency over 16% on 1 cm^2 scale. *Adv. Mater.* **29**, 1603923 (2017).
135. Lin, X. et al. Efficiency progress of inverted perovskite solar cells. *Energy Environ. Sci.* **13**, 3823–3847 (2020).
136. Seo, S., Jeong, S., Bae, C., Park, N. G. & Shin, H. Perovskite solar cells with inorganic electron- and hole-transport layers exhibiting long-term ($\approx 500\text{ h}$) stability at 85°C under continuous 1 sun illumination in ambient air. *Adv. Mater.* **30**, 1801010 (2018).
137. Brinkmann, K. O. et al. Suppressed decomposition of organometal halide perovskites by impermeable electron-extraction layers in inverted solar cells. *Nat. Commun.* **8**, 13938 (2017).
138. Zhang, S. et al. Barrier designs in perovskite solar cells for long-term stability. *Adv. Energy Mater.* **10**, 2001610 (2020).
139. Gahlmann, T. et al. Impermeable charge transport layers enable aqueous processing on top of perovskite solar cells. *Adv. Energy Mater.* **10**, 1903897 (2020).
140. Wahl, T., Hanisch, J., Meier, S., Schultes, M. & Ahlswede, E. Sputtered indium zinc oxide rear electrodes for inverted semitransparent perovskite solar cells without using a protective buffer layer. *Org. Electron.* **54**, 48–53 (2018).
141. Xu, J. et al. Triple-halide wide-band gap perovskites with suppressed phase segregation for efficient tandems. *Science* **367**, 1097–1104 (2020).
142. Liu, S. et al. Boost the efficiency of nickel oxide-based formamidinium-cesium perovskite solar cells to 21% by using coumarin 343 dye as defect passivator. *Nano Energy* **94**, 106935 (2022).
143. Liu, Z., Ono, L. K. & Qi, Y. B. Additives in metal halide perovskite films and their applications in solar cells. *J. Energy Chem.* **46**, 215–228 (2020).
144. Xiong, S. et al. Direct observation on p- to n-type transformation of perovskite surface region during defect passivation driving high photovoltaic efficiency. *Joule* **5**, 467–480 (2021).
145. Liu, K. et al. Zwitterionic-surfactant-assisted room-temperature coating of efficient perovskite solar cells. *Joule* **4**, 2404–2425 (2020).
146. Jiang, M. et al. Engineering green-to-blue emitting CsPbBr_3 quantum-dot films with efficient ligand passivation. *ACS Energy Lett.* **4**, 2731–2738 (2019).
147. Liu, C. et al. Tuning structural isomers of phenylenediammonium to afford efficient and stable perovskite solar cells and modules. *Nat. Commun.* **12**, 1–9 (2021).
148. Liu, S. et al. Effective passivation with size-matched alkyldiammonium iodide for high-performance inverted perovskite solar cells. *Adv. Funct. Mater.* **32**, 2205009 (2022).
149. Cao, Q. et al. Efficient and stable inverted perovskite solar cells with very high fill factors via incorporation of star-shaped polymer. *Sci. Adv.* **7**, eabg0633 (2021).
150. Cao, Q. et al. Star-polymer multidentate-cross-linking strategy for superior operational stability of inverted perovskite solar cells at high efficiency. *Energy Environ. Sci.* **14**, 5406–5415 (2021).
151. Du, M. et al. Surface redox engineering of vacuum-deposited NiO_x for top-performance perovskite solar cells and modules. *Joule* **6**, 1931–1943 (2022).
152. Li, Y., Xie, H., Lim, E. L., Hagfeldt, A. & Bi, D. Recent progress of critical interface engineering for highly efficient and stable perovskite solar cells. *Adv. Energy Mater.* **12**, 2102730 (2022).
153. Bi, E. et al. Efficient perovskite solar cell modules with high stability enabled by iodide diffusion barriers. *Joule* **3**, 2748–2760 (2019).
154. Khadka, D. B., Shirai, Y., Yanagida, M. & Miyano, K. Insights into accelerated degradation of perovskite solar cells under continuous illumination driven by thermal stress and interfacial junction. *ACS Appl. Energy Mater.* **4**, 11121–11132 (2021).
155. Lu, Q. et al. A review on encapsulation technology from organic light emitting diodes to organic and perovskite solar cells. *Adv. Funct. Mater.* **31**, 2100151 (2021).
156. Wong-Stringer, M. et al. High-performance multilayer encapsulation for perovskite photovoltaics. *Adv. Energy Mater.* **8**, 1801234 (2018).
157. Wu, Y. et al. Perovskite solar cells with 18.21% efficiency and area over 1 cm^2 fabricated by heterojunction engineering. *Nat. Energy* **1**, 1–7 (2016).
158. Stolterfoht, M. et al. Visualization and suppression of interfacial recombination for high-efficiency large-area pin perovskite solar cells. *Nat. Energy* **3**, 847–854 (2018).
159. Chen, H. et al. Efficient and stable inverted perovskite solar cells incorporating secondary amines. *Adv. Mater.* **31**, 1903559 (2019).
160. Niu, B. et al. Mitigating the lead leakage of high-performance perovskite solar cells via in situ polymerized networks. *ACS Energy Lett.* **6**, 3443–3449 (2021).
161. Wang, Y. et al. Cation-size mismatch and interface stabilization for efficient NiO_x -based inverted perovskite solar cells with 21.9% efficiency. *Nano Energy* **88**, 106285 (2021).
162. Zeng, H. et al. Improved performance and stability of perovskite solar modules by regulating interfacial ion diffusion with nonionic cross-linked 1D lead-iodide. *Adv. Energy Mater.* **12**, 2102820 (2022).
163. Huang, H.-H. et al. A simple one-step method with wide processing window for high-quality perovskite mini-module fabrication. *Joule* **5**, 958–974 (2021).
164. Huang, Z. et al. Releasing nanocapsules for high-throughput printing of stable perovskite solar cells. *Adv. Energy Mater.* **11**, 2101291 (2021).
165. Deng, Y. et al. Defect compensation in formamidinium-cesium perovskites for highly efficient solar mini-modules with improved photostability. *Nat. Energy* **6**, 633–641 (2021).